

Double and Quadruple Flat Bands tuned by Alternative magnetic Fluxes in Twisted Bilayer Graphene

Congcong Le,¹ Qiang Zhang,² Fan Cui,^{2,3} Xianxin Wu,^{4,*} and Ching-Kai Chiu^{1,†}

¹RIKEN Interdisciplinary Theoretical and Mathematical Sciences (iTHEMS), Wako, Saitama 351-0198, Japan

²Institute of Physics, Chinese Academy of Sciences, Beijing 100190, China

³University of Chinese Academy of Sciences, Beijing 100049, China

⁴CAS Key Laboratory of Theoretical Physics, Institute of Theoretical Physics, Chinese Academy of Sciences, Beijing 100190, China

(Dated: December 27, 2023)

Twisted bilayer graphene (TBG) can host the moiré energy flat bands with two-fold degeneracy serving as a fruitful playground for strong correlations and topological phases. However, the number of degeneracy is not limited to two. Introducing a spatially alternative magnetic field, we report that the induced magnetic phase becomes an additional controllable parameter and leads to an undiscovered generation of four-fold degenerate flat bands. This emergence stems from the band inversion at Γ point near the Fermi level with a variation of both twisted angle and magnetic phase. We present the conditions for the emergence of multi-fold degenerate flat bands, which are associated with the eigenvalue degeneracy of a Birman-Schwinger operator. Using holomorphic functions, which explain the origin of the double flat bands in the conventional TBG, we can generate analytical wave functions in the magnetic TBG to show absolute flatness with four-fold degeneracy. Moreover, we identify an orbital-related intervalley coherent state as the many-body ground state at charge neutrality. In contrast, the conventional TBG has only two moiré energy flat bands, and the highly degenerate flat bands with additional orbital channels in this magnetic platform might bring richer correlation physics.

PACS numbers: 73.43.-f, 73.20.-r, 71.20.-b

Introduction – Moiré twistrionics, focusing on the exotic properties of moiré superlattices from two-dimensional (2D) twisted van der Waals multilayers, has attracted enormous attention in contemporary research[1–10]. One well-known example is the twisted bilayer graphene (TBG), where moiré interlayer coupling can significantly alter the low-energy physics, and its electronic structure is described by the Bistritzer-MacDonald model for a small twisted angle [1]. Most prominently, when the twisted angle is adjusted to be magic values, the low-energy Dirac bands evolve to isolated two-fold flat bands (FBs) with "fragile" topology [4]. Thus, these FBs in the TBG offer an exciting playground to explore emergent correlated and topological physics, and a wide range of intriguing correlated phenomena have been experimentally observed, such as correlated insulating states[2, 5, 11–15], unconventional superconductivity[3, 5, 15–18] and quantum anomalous Hall effect[19–22].

When chiral symmetry is preserved, at magic angles the moiré FBs are absolutely flat in the entire moiré Brillouin zone (BZ). This absolute flatness can be proved by the construction of the wave functions (WFs) from holomorphic functions [23]. In addition, calculating the spectral of a compact Birman-Schwinger operator can precisely determine all real magic angles for the two-fold FBs (per valley/spin) [24, 25]. Till now, however, most studies have focused on the double FBs in the TBG because this two-fold degeneracy originates from non-degenerate bands of the Dirac cones. An interesting and outstanding question is: is it possible to realize FBs with higher degeneracy? Such an exploration is highly desirable

as this realization will not only provide new insights into the origin of magic angles and FBs but also offer a more fruitful platform hosting diversified strongly-correlated physics.

Beyond the two-fold degeneracy of the moiré FBs, in this work, we show that an undiscovered generation of FBs with four-fold degeneracy emerges in the presence of spatially alternating magnetic fields, motivated by the electronic tunability in 2D systems with external uniform magnetic fields [26–29] modified by the hexagonal Haldane model [30]. Then, the Dirac cone of the monolayer acquires an additional magnetic phase φ . Importantly, this magnetic phase expands the solutions of magic angles to the complex eigenvalues of the Birman-Schwinger operator, in contrast to the real eigenvalues of the conventional TBG. Interestingly, some complex eigenvalues correspond to quadruple FBs (per valley/spin) with absolute flatness and non-trivial topology. Moreover, to reveal the origin of the quadruple bands, we show that the WFs can be generated by holomorphic functions with two real-space nodes, and the generating functions naturally lead to absolute flatness with the four-fold degeneracy. Finally, we discuss that the four-fold degeneracy can enrich correlated physics due to additional filling selections in these multi-fold FBs.

Model—To be specific, we consider monolayer graphene with alternative magnetic fluxes in each triangle inside a hexagonal plaquette (Fig.S1(a)), similar to the Haldane model[30]. The blue (\odot) and yellow (\otimes) triangles denote outward and inward to the plane fluxes, and the total flux through each hexagonal plaquette vanishes. With a Peierls substitution, the nearest-neighbor hopping acquires a magnetic phase φ . The Dirac Hamiltonian in the real space gains an additional phase and reads (See supplemental Material (SM))

$$h_D^\varphi(\mathbf{r}) = -v_0 \begin{pmatrix} 0 & e^{-i\varphi}2\partial \\ e^{i\varphi}2\bar{\partial} & 0 \end{pmatrix}, \quad (1)$$

*Electronic address: xxwu@itp.ac.cn

†Electronic address: ching-kai.chiu@riken.jp

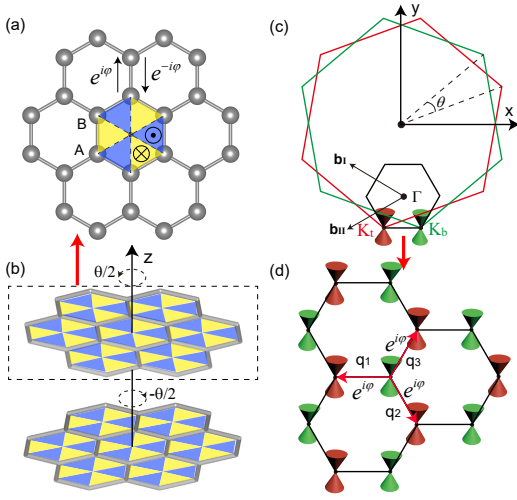


FIG. S1: (color online) (a) Distribution of periodic local magnetic fluxes in hexagonal plaquette of monolayer graphene with basis A and B. (b) TBG with alternative fluxes. (c) The two monolayer BZs with the twist form a moiré BZ. The red and green hexagons exhibit the BZs of the bottom and top layers, each rotated by an angle $\pm\theta/2$, and the black hexagon indicates the moiré BZ with momentum bases $\mathbf{b}_{I/II} = \sqrt{3}k_\theta(-\sqrt{3}/2, \pm 1/2)$. (d) The reciprocal lattice structures. The interlayer coupling with the phase φ couple the red and green Dirac cones separately located in the top and bottom layers.

with $\bar{\partial} = \frac{1}{2i}(\partial_x + i\partial_y)$ and Fermi velocity v_0 . The standard Dirac Hamiltonian is restored for monolayer graphene in the absence of magnetic flux. Then, we introduce a twist with angle θ between these two graphene layers (Fig.S1(b)). We use the basis of $\Phi(\mathbf{r}) = (e^{i\frac{\varphi}{2}}\psi_A^t, e^{i\frac{\varphi}{2}}\psi_A^b, e^{-i\frac{\varphi}{2}}\chi_B^t, e^{-i\frac{\varphi}{2}}\chi_B^b)^T$, which absorbs the magnetic phase, where t/b denotes the top/bottom graphene layers and A/B is the sublattice index. The chirally symmetric continuum model of TBG with alternating fluxes can be written as

$$H^\varphi(\mathbf{r}) = \begin{pmatrix} 0 & D^{\varphi*}(-\mathbf{r}) \\ D^\varphi(\mathbf{r}) & 0 \end{pmatrix}, \quad (2)$$

$$D^\varphi(\mathbf{r}) = \begin{pmatrix} 2\bar{\partial} & e^{i(\varphi+\beta)}\alpha_0 U(\mathbf{r}) \\ e^{i(\varphi-\beta)}\alpha_0 U(-\mathbf{r}) & 2\bar{\partial} \end{pmatrix}, \quad (3)$$

where $U(\mathbf{r}) = e^{-i\mathbf{q}_1 \cdot \mathbf{r}} + e^{-i\mathbf{q}_2 \cdot \mathbf{r}}e^{i\phi} + e^{-i\mathbf{q}_3 \cdot \mathbf{r}}e^{-i\phi}$ with $\phi = 2\pi/3$. $\mathbf{q}_1 = k_\theta(-1, 0)$, $\mathbf{q}_{2,3} = k_\theta(1/2, \mp\sqrt{3}/2)$ are shown in Fig.S1(d) with $k_\theta = 2k_D \sin(\theta/2)$, and $k_D = |\mathbf{K}_{t/b}|$ is Dirac momentum in the monolayer graphene. The above Hamiltonian is characterized by a dimensionless real parameter $\alpha_0 e^{i\beta} = \frac{\omega_{AB}}{v_0 k_\theta}$, where ω_{AB} is the strength of the interlayer coupling with a constant phase β . Unlike the magnetic phase φ , the global phase β can be gauged away. For simplicity, we define a complex parameter $\alpha(\varphi) \equiv \alpha_0 e^{i\varphi}$. In addition, $H^\varphi(\mathbf{r})$ is off-diagonal as we consider the chiral limit, where we neglect intra-sublattice (AA/BB) interlayer hopping. Since the twisted angle is small, we also neglect the rotation effect on the Dirac Hamiltonian $h_D^\varphi(\mathbf{r})$ [23]. In the momen-

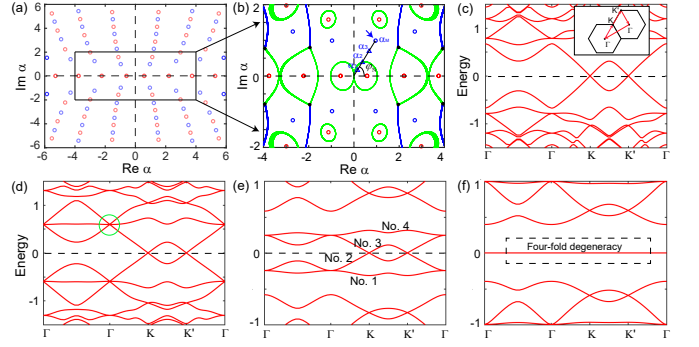


FIG. S2: (color online) (a) The spectra \mathcal{A} shows the magic values of the dimensionless complex parameter α corresponding to double (red) and quadruple (blue) FBs. (b) The distribution of lowest energy band touching at Γ point in the spectra \mathcal{A} . The band structures of the Hamiltonian $H^\varphi(\mathbf{r})$ with magnetic phase $\varphi_N = 0.254\pi$ in the different α_0 values marked by blue triangle in (b): (c) $\alpha_1 = 0.3e^{i\varphi_N}$, (d) $\alpha_2 = 0.55e^{i\varphi_N}$, (e) $\alpha_3 = 1.0e^{i\varphi_N}$ and (f) $\alpha_M = 1.379e^{i\varphi_N}$. The inset in (c) indicates the spectrum path in the moiré BZ. The green circle in (d) denotes band inversion between double degenerate and non-degenerate points at Γ .

tum space, the interlayer coupling $U(\mathbf{r})$ can be illustrated by the network of the two Dirac cones with the extension of the momentum hoppings, where the hopping between the nearest-neighbor momentum sites acquires a phase $e^{i\varphi}$ owing to the alternative fluxes (Fig.S1(c) and (d)). This non-zero phase plays a pivotal role in generating multi-fold FBs.

Multi-fold FBs– We further discuss the conditions of absolutely zero-energy FBs for the above continuum model. After a gauge transformation $V = \text{diag}(e^{-i\mathbf{k} \cdot \mathbf{r}}, e^{-i\mathbf{k} \cdot \mathbf{r}})$, the Hamiltonian $H_k^\varphi(\mathbf{r}) = V^\dagger H^\varphi(\mathbf{r})V$ can be written as

$$H_k^\varphi(\mathbf{r}) = \begin{pmatrix} 0 & D_k^{\varphi*}(-\mathbf{r}) \\ D_k^\varphi(\mathbf{r}) & 0 \end{pmatrix}, \quad (4)$$

where $D_k^\varphi(\mathbf{r}) \equiv D^\varphi(\mathbf{r}) - \mathbf{k}$ and the momentum \mathbf{k} is defined in moiré BZ. The explicit form of $D_k^\varphi(\mathbf{r})$ is given by

$$D_k^\varphi(\mathbf{r}) = (2\bar{\partial} - \mathbf{k})(I + \alpha(\varphi)T_k), \\ T_k = (2\bar{\partial} - \mathbf{k})^{-1} \begin{pmatrix} 0 & U(\mathbf{r}) \\ U(-\mathbf{r}) & 0 \end{pmatrix}, \quad (5)$$

where T_k ($\mathbf{k} \neq 0$) is known as the Birman-Schwinger operator [24, 25]. The appearance of zero-energy FBs implies that the determinant of Hamiltonian $H_k^\varphi(\mathbf{r})$ vanishes for all \mathbf{k} , i.e. $\det(D_k^\varphi(\mathbf{r})) = 0$. Due to $\det(2\bar{\partial} - \mathbf{k}) \neq 0$, for all non-zero \mathbf{k} the matrix $[I - \alpha(\varphi)T_k]$ should have at least one zero eigenvalue and for $\mathbf{k} = 0$ two low-energy states are fixed at zero energy. According to Ref.[24, 25], the eigenvalues of T_k are independent of \mathbf{k} and we can define a spectrum $\mathcal{A} = 1/\text{Spec}(T_k)$ and a corresponding two-component eigenstate $\psi_k^0(\mathbf{r})$. Therefore, once the parameter α is tuned to be one of the complex eigenvalues in \mathcal{A} , $D_k^\varphi(\mathbf{r})\psi_k^0(\mathbf{r}) = 0$ so that zero-energy FBs emerge in $H_k^\varphi(\mathbf{r})$ and α has a magic value.

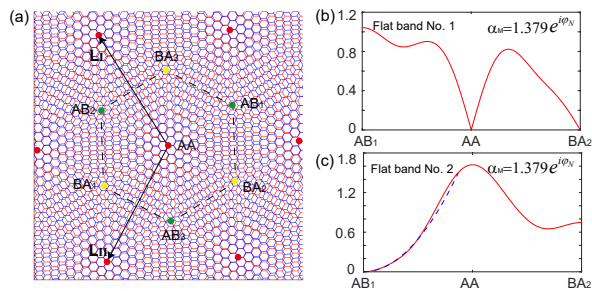


FIG. S3: (color online) (a) Schematic moiré pattern. The red, green and yellow points indicate the AA, AB and BA stacking points, and $\mathbf{L}_{I/II} = 4\pi/3k_\theta(-1/2, \pm\sqrt{3}/2)$ are moiré lattice vector. (b) and (c) The norm of the 2-component WFs $\psi_{\mathbf{K},1/2}(\mathbf{r})$ at \mathbf{K} point for FB No.1/2 at magic α_M . The blue dashed line in (c) represents the fitting of quadratic function.

In the absence of the alternative magnetic field ($\varphi = 0$), the magic parameters α in the conventional TBG appear recursively on the real axis of spectrum \mathcal{A} [24, 25], and indicate the presence of double FBs (Fig.S2(a)). When the alternative magnetic field is recovered, the magic values of α are expanded to the entire complex plane. The spectrum \mathcal{A} exhibit no degeneracy (red circles) and two-fold degeneracy (blue circles), respectively (Fig.S2(a)). The non-degenerate and two-fold degenerate eigenvalues correspond to double and quadruple FBs in magnetic TBG (see SM). That is, the degeneracy of FBs is twice the degeneracy at magic values. Introducing the alternative fluxes extends magic parameters to more discrete values and leads to the emergence of quadruple FBs.

To investigate the evolution of the degeneracy in the spectra of the magnetic TBG, we take the complex eigenvalue closest to the origin in Fig.S2(b) as a example with magnetic phase $\varphi_N = 0.254\pi$ to demonstrate the changes of the low energy bands. The degeneracy of FBs is intimately related to the degeneracy of the lowest energy states at Γ in the TBG spectrum. To understand the transition of FBs with different degeneracies as α varies, we can track the band touch of the low-energy states at Γ (Fig.S2(b)). The green (blue) curves represent a three-fold (four-fold) band touching at Γ , resulting in band inversions between one singlet and one doublet (between two doublets). Importantly, the three-fold degeneracy curves (Fig.S2(d)) separate the magic parameters α with double and quadruple FBs. Inside one of these degeneracy loops, two connected bands near zero energy in a direct gap (Fig.S2(c)) evolve to double FBs at magic α (red circles). As α crosses a three-fold degeneracy line, the band inversion changes two connected bands to four connected ones in the gap (Fig.S2(e)). Outside these degeneracy loops, the four connected bands evolve to quadruple FBs (Fig.S2(f)) at magic α (blue circles). Then, as discussed in SM, we consider the effect of intra-sublattice interlayer coupling, which can result in a slight dispersion of the quadruple FBs. In addition, within the quadruple FBs, two of them (No.2/3) that constitute Dirac points possess exhibit Chern numbers of ± 1 while the Chern numbers of the remaining two bands (No.1/4) vanish.

Origin of quadruple FBs– In the conventional TBG, the key to rigorously showing the emergence of the double absolutely FBs is that at the magic angles, the absolute values of the WFs with the zero energy at \mathbf{K}/\mathbf{K}' have a linear-momentum-dispersion node at BA/AB stacking (Fig.S3(a)). Using this WF at \mathbf{K} , one generates two eigenfunctions with zero energy at any momentum point [23]. For the magnetic TBG, we can use a similar approach to show the absolute flatness of the quadruple bands at magic α by identifying the nodes of the WFs at \mathbf{K} and extending this function to the entire Moiré BZ.

To distinguish the quadruple FBs, consider α slightly away from the magic value (Fig.S2(e)). The two lowest bands are labeled by No.1/2, and the remaining two bands can be generated by chiral symmetry operator $S = \tau_z \sigma_0$. In addition, due to C_2T symmetry, the non-degenerate 4-component WF $\Psi_{\mathbf{k},i}(\mathbf{r})$ can be expressed by a 2-component vector $\psi_{\mathbf{k},i}(\mathbf{r})$ with band index $i = 1, 2$. At the magic $\alpha_M = 1.379e^{i\varphi_N}$, the norm $[\psi_{\mathbf{K},1/2}^\dagger(\mathbf{r})\psi_{\mathbf{K},1/2}(\mathbf{r})]^{1/2}$ shows that for FB No.1 at \mathbf{K} , two nodes appear at the AA and BA stacking with a dominant linear real-space dependence (Fig.S3(b)). Meanwhile, for FB No.2 at \mathbf{K} , there is only one node at the AB stacking, and the norm exhibits real-space quadratic dependence near it, implying a second order node (Fig.S3(c)). These nodal features in sharp contrast to the conventional TBG are the important ingredients for the absolute flatness of the quadruple bands.

To simplify the absolute flatness' problem, we focus on the solution of $D^\varphi(\mathbf{r})\psi_{\mathbf{k}}(\mathbf{r}) = 0$ for all \mathbf{k} . Previously, we numerically obtain the two-component WFs $\psi_{\mathbf{k}}(\mathbf{r})$ pinned at zero energy at \mathbf{K} , which is a good starting point to construct WFs of the FBs at other \mathbf{k} . As $\mathbf{k} \neq \mathbf{K}$, the conjectural WF can be written as $\psi_{\mathbf{k}}(\mathbf{r}) \equiv f_{\mathbf{k}}(z)\psi_{\mathbf{K}}(\mathbf{r})$ with $z = x + iy$ since $D^\varphi(\mathbf{r})\psi_{\mathbf{k}}(\mathbf{k}) = f_{\mathbf{k}}(z)[D^\varphi(\mathbf{r})\psi_{\mathbf{K}}(\mathbf{r})] = 0$. The holomorphic function $f_{\mathbf{k}}(z)$ is either a constant or unbounded by Liouville's theorem, indicating that $f_{\mathbf{k}}(z)$ is meromorphic and thus has poles as $\mathbf{k} \neq \mathbf{K}$. The eigenfunctions $\psi_{\mathbf{k}}(\mathbf{r})$ are valid when the poles of $f_{\mathbf{k}}(z)$ are smoothed out by the nodes of $\psi_{\mathbf{K}}(\mathbf{r})$ in the Moiré unit cell. For the double FBs in the conventional TBG, only one node appears in $\psi_{\mathbf{K}}(\mathbf{r})$. Differently, for the quadruple FBs, a second-order node at AB stacking point emerges in $\psi_{\mathbf{K},2}(\mathbf{r})$ of the band No.2 at the magic α , while there are already two linear nodes in the $\psi_{\mathbf{K},1}(\mathbf{r})$ of the band No.1. We note that $\psi_{\mathbf{K},2}(\mathbf{r})$ is always pinned at the zero-energy and possesses the node only at the magic α . In contrast, $\psi_{\mathbf{K},1}(\mathbf{r})$ always has the two nodes and drops to zero energy at the magic α . The zero energy and the presence of the nodes at the magic α lead to the solution of the zero-energy absolutely FBs in the entire Moiré BZ.

We turn to the construction of WFs for the quadruple FBs. To cancel the poles of $\Psi_{\mathbf{K}}(\mathbf{r})$, we choose two theta functions in the denominator of $f_{\mathbf{k}}(z)$ and adjust $f_{\mathbf{k}}(z)$ to render the two-component WF $\psi_{\mathbf{k}}(\mathbf{r})$ to obey the Bloch boundary conditions on moiré lattice vectors $\mathbf{L}_{I/II}$, namely $\psi_{\mathbf{k}}(\mathbf{r} + \mathbf{L}_{I/II}) = e^{i\mathbf{k}\cdot\mathbf{L}_{I/II}}U\psi_{\mathbf{k}}(\mathbf{r})$ with $U = \text{diag}(e^{-i\phi}, e^{i\phi})$ [23]. The analytical

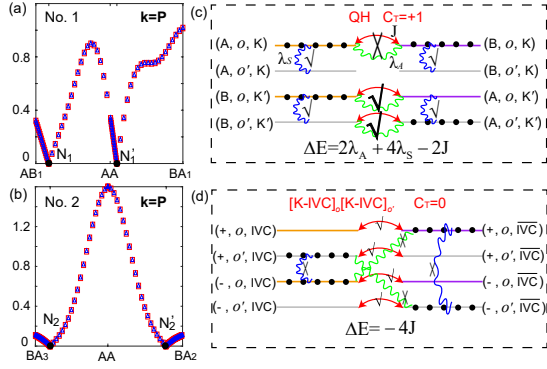


FIG. S4: (color online) (a) and (b) The norm of WFs $\psi_{\mathbf{k},1/2}(\mathbf{r})$ for FBs No.1/2 at $\mathbf{k} = \mathbf{P}$ with $\mathbf{P} = 0.5\mathbf{b}_I - 0.3\mathbf{b}_{II}$. $N_{1/2}$ and $N'_{1/2}$ are corresponding nodal points. (c) and (d) The configurations for QH and $[K-IVC]_o[K-IVC]_{o'}$ states with $C_T = +1$ and $C_T = 0$, and the IVC bases are a coherent superposition of two valley FB bases and the relations can be found in SM. The FBs labelled by gray, orange and pink lines possess Chern number $C = 0$, $C = +1$, and $C = -1$. The symbols \surd or \times indicate whether the processes are permitted or forbidden.

expressions for the quadruple FB WFs $\Psi_{\mathbf{k},1/2}(\mathbf{r})$ read,

$$\Psi_{\mathbf{k},1}(\mathbf{r}) = \frac{\vartheta_{a_1, b_1}(\nu|\omega)\vartheta_{a'_1, b'_1}(\nu|\omega)}{\vartheta_{\frac{1}{2}, \frac{1}{2}}(\nu|\omega)\vartheta_{\frac{5}{6}, \frac{7}{6}}(\nu|\omega)}\Psi_{\mathbf{K},1}(\mathbf{r}), \quad (6)$$

$$\Psi_{\mathbf{k},2}(\mathbf{r}) = \frac{\vartheta_{a_2, b_2}(\nu|\omega)\vartheta_{a'_2, b'_2}(\nu|\omega)}{[\vartheta_{\frac{7}{6}, \frac{5}{6}}(\nu|\omega)]^2}\Psi_{\mathbf{K},2}(\mathbf{r}), \quad (7)$$

with $\nu = z/L_I$, $\omega = \frac{L_{II}}{L_I} = e^{i\phi}$ and $L_{II} = (\mathbf{L}_{II})_x + i(\mathbf{L}_{II})_y$. To satisfy the Bloch boundary conditions, the rational characteristics a and b obey

$$a_i + a'_i = \frac{1}{3} + \frac{(\mathbf{k} - \mathbf{K}) \cdot \mathbf{L}_I}{2\pi} + n_I, \quad (8)$$

$$b_i + b'_i = \frac{2}{3} - \frac{(\mathbf{k} - \mathbf{K}) \cdot \mathbf{L}_{II}}{2\pi} + n_{II}, \quad (9)$$

where n_I and n_{II} are arbitrary integers due to the lattice translational symmetry. The definition of the theta function $\vartheta_{a,b}(\nu|\omega)$ and the detailed derivations of Eq.6/7 are provided in the SM. The equations above cannot determine the explicit expressions of the rational characteristics, which are functions of \mathbf{k} , unless the node locations are given.

To prove the absolutely FBs, we numerically calculate the flat-band WFs from Hamiltonian $H^\varphi(\mathbf{r})$ and determine the node locations. The node locations fix the values of a , b in theta functions Eq.6/7. To confirm the validity of the WF expressions in Eq.6/7, we first select a general point \mathbf{P} as an example. Fig.S8 (a) and (b) show the norm of WFs $\psi_{\mathbf{k},1/2}$ for FB No.1/2 at $\mathbf{k} = \mathbf{P}$, where the WFs from Hamiltonian $H^\varphi(\mathbf{r})$ and Eq.6/7 are labelled in red squares and blue triangles, respectively. We find a good agreement between them, and the agreement can be extended to other general \mathbf{k} points (see SM). Therefore, through the evolution of nodes and real-space WF, we have verified the validity of WF in Eq.6/7, and

quadruple FBs are absolutely flat. In SM, we further confirm the validity of the relation between Eq.8/9 and nodal coordinates.

Correlation states—The presence of multiple-fold FBs provides an excellent platform for exploring correlated quantum states. Besides the valley and sublattice degrees of freedom in double FBs [6], the quadruple FBs introduce an emergent orbital degree of freedom, which can significantly enrich the correlated states. Within the quadruple FBs, two of them (No.2/3) that constitute Dirac points possess exhibit Chern numbers of ± 1 labeled by o -orbital while the Chern numbers of the remaining two bands (No.1/4 o' -orbital) vanish. Therefore, in the spinless case with the two valleys, the total Chern numbers of ± 2 can be realized in the Quantum Hall (QH) states at integer filling[6, 32, 33]. With a fractional filling of the high-Chern-number FBs[34], fractional quantum Hall states at a variety of filling factors can be realized. We use the half-filling scenario (four out of the eight FBs are filled) as an primary example. Assuming the intrasublattice-intraorbital interaction scale is much larger than other scales, the ground state of this interaction is the one where each of the eight bands is completely filled or empty [6]. There are $C_4^8 = 70$ degenerate many-body ground states (see SM), while only $C_2^4 = 6$ ground states are present in the conventional TBG. However, for intervalley-coherent (IVC) states, the types of ground states increase significantly, and an exotic combination of the QH and IVC states, such as time-reversal IVC (T-IVC) and Kramers IVC (K-IVC) states, can be realized (see SM) [6]. We schematically show the two representative examples: orbital related QH and $[K-IVC]_o[K-IVC]_{o'}$ states in Fig.4 (c) and (d). The former state features three fully occupied o -orbital FBs and one fully occupied o' -orbital FB, where the o -orbital can contribute to the Chern number $C_T = +1$. In the latter state, both o and o' orbital sectors feature K-IVC states with anti-parallel pseudospin between two orbitals.

Now we introduce the effect of single-particle dispersion, intersublattice-intraorbital interaction and intrasublattice-interorbital interaction as perturbations, so the high degeneracy of the ground states can be lifted. The single-particle dispersion introduces a hopping between the horizontal pair states ($A \leftrightarrow B$) (denoted by red curves in Fig.S8(c)), yielding a energy reduction of the order of J . For the latter two interaction terms, the corresponding energy increments are proportional to $\lambda_{A/S} \sum_{i=1,2} \hat{n}_i(1 - \hat{n}_i)$, where \hat{n}_i is the particle number operator for one of horizontal ($A \leftrightarrow B$) or vertical ($o \leftrightarrow o'$) pair states. They are denoted by green and blue wavy lines in Fig.S8 (c) and (d), respectively. It is evident that three types of energy corrections are nonzero when only one of the pair states is occupied. Therefore, the energy correction can be formulated as $\Delta E = N_A \lambda_A + N_S \lambda_S - N_J J$ [35]. From the energy, we identify the anti-orbital K-IVC state in Fig.S8(d) as the ground state at charge neutrality. Varying doping and twisted angles may induce transitions between different correlated states, necessitating detailed Hartree Fock calculations, which we defer to future investigations.

Discussion and conclusion—In recent experiments, FBs have been successfully achieved in twisted-bilayer optical lattice systems[36]. Our proposed model can be implemented

within this tunable optical lattice platform, thanks to its large spatial scale, making it possible to achieve alternative magnetic field. In summary, introducing alternative fluxes opens a venue for undiscovered multiple magic angles and another generation of absolutely FBs with higher degeneracy. Specifically, we report that the double and quadruple FBs appear recursively in TBG with alternative magnetic fluxes, and adjusting the twisted angle and magnetic phase can control the transition between double and quadruple FBs. The quadruple FBs share the same origin with the conventional TBG, and by us-

ing holomorphic functions, we can generate analytical WFs to show the absolute flatness of the quadruple bands. Moreover, additional orbitals in the quadruple bands lead to more diversified strongly correlated physics. Our work demonstrates that the magnetic phase is a unique tuning parameter to tailor the electronic structure in moiré twistrionics, which can significantly enrich topological and correlated phenomena.

Acknowledgments– We thank Zhida Song, Simon Becker and Xu Zhang for the helpful discussions and comments. C.-K.C. was supported by JST Presto Grant No. JPMJPR2357.

-
- [1] R. Bistritzer and A. H. MacDonald, *Proc. Natl. Acad. Sci.* **108**, 12233 (2011).
- [2] Y. Cao, V. Fatemi, A. Demir, S. Fang, S. L. Tomarken, J. Y. Luo, J. D. Sanchez-Yamagishi, K. Watanabe, T. Taniguchi, E. Kaxiras, R. C. Ashoori, and P. Jarillo-Herrero, *Nature* **556**, 80 (2018).
- [3] Y. Cao, V. Fatemi, S. Fang, K. Watanabe, T. Taniguchi, E. Kaxiras, and P. Jarillo-Herrero, *Nature* **556**, 43 (2018).
- [4] H. C. Po, L. Zou, A. Vishwanath, and T. Senthil, *Phys. Rev. X* **8**, 031089 (2018).
- [5] X. Lu, P. Stepanov, W. Yang, M. Xie, M. A. Aamir, I. Das, C. Urgell, K. Watanabe, T. Taniguchi, G. Zhang, A. Bachtold, A. H. MacDonald, and D. K. Efetov, *Nature* **574**, 653 (2019).
- [6] G. Chen, L. Jiang, S. Wu, B. Lyu, H. Li, B. L. Chittari, K. Watanabe, T. Taniguchi, Z. Shi, J. Jung, Z. Yuanbo, and W. Feng, *Nature Physics* **15**, 237 (2019).
- [7] G. Chen, A. L. Sharpe, P. Gallagher, I. T. Rosen, E. J. Fox, L. Jiang, B. Lyu, H. Li, K. Watanabe, T. Taniguchi, J. Jung, Z. Shi, D. Goldhaber-Gordon, Y. Zhang, and F. Wang, *Nature* **572**, 215 (2019).
- [8] T. Devakul, V. Crépel, Y. Zhang, and L. Fu, *Nature Communications* **12**, 6730.
- [9] A. Ghiotto, E.-M. Shih, G. S. Pereira, D. A. Rhodes, B. Kim, J. Zang, A. J. Millis, K. Watanabe, T. Taniguchi, J. C. Hone, L. Wang, C. R. Dean, and A. N. Pasupathy, *Nature* **597**, 345 (2021).
- [10] P. J. Ledwith, A. Vishwanath, and E. Khalaf, *Phys. Rev. Lett.* **128**, 176404 (2022).
- [11] C. Shen, Y. Chu, Q. Wu, N. Li, S. Wang, Y. Zhao, J. Tang, J. Liu, J. Tian, K. Watanabe, T. Taniguchi, R. Yang, Z. Y. Meng, D. Shi, O. V. Yazyev, and G. Zhang, *Nature Physics* **16**, 520 (2020).
- [12] U. Zondiner, A. Rozen, D. Rodan-Legrain, Y. Cao, R. Queiroz, T. Taniguchi, K. Watanabe, Y. Oreg, F. von Oppen, A. Stern, E. Berg, P. Jarillo-Herrero, and S. Ilani, *Nature* **582**, 203 (2020).
- [13] D. Wong, K. P. Nuckolls, M. Oh, B. Lian, Y. Xie, S. Jeon, K. Watanabe, T. Taniguchi, B. A. Bernevig, and A. Yazdani, *Nature* **582**, 198 (2020).
- [14] I. Das, C. Shen, A. Jaoui, J. Herzog-Arbeitman, A. Chew, C.-W. Cho, K. Watanabe, T. Taniguchi, B. A. Piot, B. A. Bernevig, and D. K. Efetov, *Phys. Rev. Lett.* **128**, 217701 (2022).
- [15] M. Christos, S. Sachdev, and M. S. Scheurer, *Phys. Rev. X* **12**, 021018 (2022).
- [16] J. M. Park, Y. Cao, K. Watanabe, T. Taniguchi, and P. Jarillo-Herrero, *Nature* **590**, 249 (2021).
- [17] M. Yankowitz, S. Chen, H. Polshyn, Y. Zhang, K. Watanabe, T. Taniguchi, D. Graf, A. F. Young, and C. R. Dean, *Science* **363**, 1059 (2019).
- [18] P. Stepanov, I. Das, X. Lu, A. Fahimniya, K. Watanabe, T. Taniguchi, F. H. Koppens, J. Lischner, L. Levitov, and D. K. Efetov, *Nature* **583**, 375 (2020).
- [19] M. Serlin, C. L. Tschirhart, H. Polshyn, Y. Zhang, J. Zhu, K. Watanabe, T. Taniguchi, L. Balents, and A. F. Young, *Science* **367**, 900 (2020).
- [20] A. L. Sharpe, E. J. Fox, A. W. Barnard, J. Finney, K. Watanabe, T. Taniguchi, M. A. Kastner, and D. Goldhaber-Gordon, *Science* **365**, 605 (2019).
- [21] W.-Y. He, D. Goldhaber-Gordon, and K. T. Law, *Nature Communications* **11**, 1650 (2020).
- [22] C.-C. Tseng, X. Ma, Z. Liu, K. Watanabe, T. Taniguchi, J.-H. Chu, and M. Yankowitz, *Nature Physics* **18**, 1038 (2022).
- [23] G. Tarnopolsky, A. J. Kruchkov, and A. Vishwanath, *Phys. Rev. Lett.* **122**, 106405 (2019).
- [24] S. Becker, M. Embree, J. Wittsten, and M. Zworski, *Phys. Rev. B* **103**, 165113 (2021).
- [25] S. Becker, M. Embree, J. Wittsten, and M. Zworski, *Probability and Mathematical Physics* **3**, 69 (2022).
- [26] V. o. T. Phong and E. J. Mele, *Phys. Rev. Lett.* **128**, 176406 (2022).
- [27] J. Dong, J. Wang, and L. Fu, *arXiv:2208.10516* (2022).
- [28] J. Herzog-Arbeitman, A. Chew, and B. A. Bernevig, *Phys. Rev. B* **106**, 085140 (2022).
- [29] Y. Guan, O. V. Yazyev, and A. Kruchkov, *Phys. Rev. B* **106**, L121115 (2022).
- [30] F. D. M. Haldane, *Phys. Rev. Lett.* **61**, 2015 (1988).
- [6] N. Bultinck, E. Khalaf, S. Liu, S. Chatterjee, A. Vishwanath, and M. P. Zaletel, *Phys. Rev. X* **10**, 031034 (2020).
- [32] Y.-H. Zhang, D. Mao, Y. Cao, P. Jarillo-Herrero, and T. Senthil, *Phys. Rev. B* **99**, 075127 (2019).
- [33] Y.-H. Zhang, D. Mao, and T. Senthil, *Phys. Rev. Research* **1**, 033126 (2019).
- [34] P. J. Ledwith, G. Tarnopolsky, E. Khalaf, and A. Vishwanath, *Phys. Rev. Research* **2**, 023237 (2020).
- [35] The parameters $N_{A/S/J}$ are determined by the number of active interacting and hopping channels between pair states and $\lambda_{A/S}, J > 0$.
- [36] Z. Meng, L. Wang, W. Han, F. Liu, K. Wen, C. Gao, P. Wang, C. Chin, and J. Zhang, *Nature* **615**, 231 (2023).

Contents

References	5
A. Effective model, symmetry analysis, topological property and condition for multi-fold degenerate flat bands	6
1. Chirally symmetric continuum model	6
2. Approximate symmetry in the low energy	8
3. Symmetry correspondence between momentum space and real space	9
4. Topological property	9
5. Condition for the emergence of multi-fold degenerate flat bands	9
6. Effect of the intra-sublattice interlayer coupling	11
B. Theta function and flat band wave function	12
1. Theta function	12
2. Wave function for quadruple flat bands	12
3. Nodal evolution in real space	14
C. Ground states of TBG with alternative magnetic fluxes at half-filling	16
1. Projected interaction and ground states	16
a. Projected interaction	16
b. Ground states of intrasublattice-intraorbital interaction	17
2. Energy correction of ground states	20
a. Single-particle dispersion	20
b. Intersublattice-intraorbital interaction	22
c. Intrasublattice-interorbital interaction	25
d. Intuitive picture about the energy correction	28
References	30

Appendix A: Effective model, symmetry analysis, topological property and condition for multi-fold degenerate flat bands

In this section, we provide a comprehensive derivation of the chirally symmetric continuum model that describes twisted bilayer graphene (TBG) under a periodic alternating magnetic field. We engage in an in-depth analysis of the symmetry associated with this system, including approximate symmetries in the low energy and correspondence of symmetries between momentum space and real space. Furthermore, we elucidate the conditions for the emergence of multi-fold degenerate flat bands, and topological properties for the flat bands. In addition, we analyze the impact of intra-sublattice interlayer coupling on these flat bands.

1. Chirally symmetric continuum model

The monolayer graphene, composed of sublattices A and B as depicted in Fig.S5(a), is characterized by translation vectors $\mathbf{a}_1 = a(-\frac{1}{2}, \frac{\sqrt{3}}{2})$ and $\mathbf{a}_2 = a(-\frac{1}{2}, -\frac{\sqrt{3}}{2})$, where a denotes the lattice constant. The corresponding reciprocal vectors, illustrated in Fig.S5(b), are $\mathbf{b}_1 = \frac{4\pi}{a\sqrt{3}}(-\frac{\sqrt{3}}{2}, \frac{1}{2})$ and $\mathbf{b}_2 = \frac{4\pi}{a\sqrt{3}}(-\frac{\sqrt{3}}{2}, -\frac{1}{2})$. It is a well-established fact that two Dirac points are located at \mathbf{K} and \mathbf{K}' points in monolayer graphene. Through the utilization of the p_z orbital, a tight-binding Hamiltonian can be established to describe Dirac points, which can be expressed as follows

$$H(\mathbf{k}) = \begin{pmatrix} 0 & h_{12}(\mathbf{k}) \\ h_{12}^*(\mathbf{k}) & 0 \end{pmatrix}, \quad (\text{A1})$$

where $h_{12}(\mathbf{k}) = t(e^{i\mathbf{k}\cdot\delta_1} + e^{i\mathbf{k}\cdot\delta_2} + e^{i\mathbf{k}\cdot\delta_3})$ with t representing the nearest-neighbor hopping along the δ bonds. These bonds are defined by vectors $\delta_1 = a(\frac{1}{2}, -\frac{\sqrt{3}}{6})$, $\delta_2 = a(0, \frac{\sqrt{3}}{3})$ and $\delta_3 = a(-\frac{1}{2}, -\frac{\sqrt{3}}{6})$, as illustrated in Fig. S5(a). By conducting a first-order expansion of Eq.A1 around \mathbf{K} and implementing a gauge transformation denoted as $g = \text{diag}(e^{-i\frac{\pi}{3}}, e^{i\frac{\pi}{3}})$, we can get the standard Dirac Hamiltonian $h_D(\mathbf{K} + \mathbf{k}) = -v_0(\sigma_x \mathbf{k}_x + \sigma_y \mathbf{k}_y)$ with Dirac velocity $v_0 = -\frac{\sqrt{3}}{2}t$.

We explore the influence of an periodic alternative magnetic fluxes in monolayer graphene, as shown in Fig.S5(a). In this depiction, the blue region (\odot) corresponds to outward-to-the-plane magnetic fluxes, while the yellow region (\otimes) signifies

inward-to-the-plane magnetic fluxes. The presence of the alternating magnetic fluxes introduces a magnetic phase φ into the nearest-neighbor hopping process, and subsequently the tight-binding Hamiltonian Eq.A1 becomes

$$H^\varphi(\mathbf{k}) = \begin{pmatrix} 0 & e^{i\varphi} h_{12}(\mathbf{k}) \\ e^{-i\varphi} h_{12}^*(\mathbf{k}) & 0 \end{pmatrix}. \quad (\text{A2})$$

Then, the corresponding Dirac Hamiltonian around \mathbf{K} becomes

$$h_D^\varphi(\mathbf{K} + \mathbf{k}) = -v_0 \begin{pmatrix} 0 & e^{i\varphi}(\mathbf{k}_x - i\mathbf{k}_y) \\ e^{-i\varphi}(\mathbf{k}_x + i\mathbf{k}_y) & 0 \end{pmatrix}. \quad (\text{A3})$$

In the real space, the Hamiltonian $h_D^\varphi(\mathbf{K} + \mathbf{k})$ can be written as

$$h_D^\varphi(\mathbf{r}) = -v_0 \begin{pmatrix} 0 & e^{i\varphi} 2\partial \\ e^{-i\varphi} 2\bar{\partial} & 0 \end{pmatrix}, \quad (\text{A4})$$

where $\partial = \frac{1}{2i}(\partial_x - i\partial_y)$ and $\bar{\partial} = \frac{1}{2i}(\partial_x + i\partial_y)$. Similar to conventional TBG[1], in the basis $\Phi(\mathbf{r}) = (\psi_A^t, \chi_B^t, \psi_A^b, \chi_B^b)^T$ with layer index t/b , the chirally symmetric model of TBG with magnetic phase can be written as

$$H^\varphi(\mathbf{r}) = \begin{pmatrix} 0 & e^{i\varphi} 2\partial & 0 & e^{i\beta} \alpha_0 U^*(-\mathbf{r}) \\ e^{-i\varphi} 2\bar{\partial} & 0 & e^{i\beta} \alpha_0 U(\mathbf{r}) & 0 \\ 0 & e^{-i\beta} \alpha_0 U^*(\mathbf{r}) & 0 & e^{i\varphi} 2\partial \\ e^{-i\beta} \alpha_0 U(-\mathbf{r}) & 0 & e^{-i\varphi} 2\bar{\partial} & 0 \end{pmatrix}, \quad (\text{A5})$$

where $U(\mathbf{r}) = e^{-i\mathbf{q}_1 \cdot \mathbf{r}} + e^{-i\mathbf{q}_2 \cdot \mathbf{r}} e^{i\phi} + e^{-i\mathbf{q}_3 \cdot \mathbf{r}} e^{-i\phi}$ with $\phi = 2\pi/3$, $\mathbf{q}_1 = k_\theta(-1, 0)$ and $\mathbf{q}_{2,3} = k_\theta(1/2, \mp\sqrt{3}/2)$. The above Hamiltonian $H^\varphi(\mathbf{r})$ is characterized by a dimensionless real parameter $\alpha_0 e^{i\beta} = \frac{\omega_{AB}}{v_0 k_\theta} \beta$, where ω_{AB} is the strength of the interlayer coupling with a constant phase β . Unlike the magnetic phase φ , the global phase β can be gauged away. By reshuffling the basis to $\Phi(\mathbf{r}) = (\psi_A^t, \psi_A^b, \chi_B^t, \chi_B^b)^T$, and performing gauge transformation $g_\varphi = \text{diag}(e^{i\frac{\varphi}{2}}, e^{i\frac{\varphi}{2}}, e^{-i\frac{\varphi}{2}}, e^{-i\frac{\varphi}{2}})$ the Hamiltonian $H^\varphi(\mathbf{r})$ Eq.A5 reads

$$H^\varphi(\mathbf{r}) = \begin{pmatrix} 0 & 0 & 2\partial & e^{i(-\varphi+\beta)} \alpha_0 U^*(-\mathbf{r}) \\ 0 & 0 & e^{i(-\varphi-\beta)} \alpha_0 U^*(\mathbf{r}) & 2\bar{\partial} \\ 2\bar{\partial} & e^{i(\varphi+\beta)} \alpha_0 U(\mathbf{r}) & 0 & 0 \\ e^{i(\varphi-\beta)} \alpha_0 U(-\mathbf{r}) & 2\bar{\partial} & 0 & 0 \end{pmatrix}. \quad (\text{A6})$$

Then, under gauge transformation $g_\beta = \text{diag}(e^{-i\frac{\beta}{2}}, e^{i\frac{\beta}{2}}, e^{-i\frac{\beta}{2}}, e^{i\frac{\beta}{2}})$, the global phase β can be gauged away, and finally the Hamiltonian $H^\varphi(\mathbf{r})$ becomes

$$H^\varphi(\mathbf{r}) = \begin{pmatrix} 0 & D^{\varphi*}(-\mathbf{r}) \\ D^\varphi(\mathbf{r}) & 0 \end{pmatrix}, D^\varphi(\mathbf{r}) = \begin{pmatrix} 2\bar{\partial} & \alpha(\varphi)U(\mathbf{r}) \\ \alpha(\varphi)U(-\mathbf{r}) & 2\bar{\partial} \end{pmatrix}, \quad (\text{A7})$$

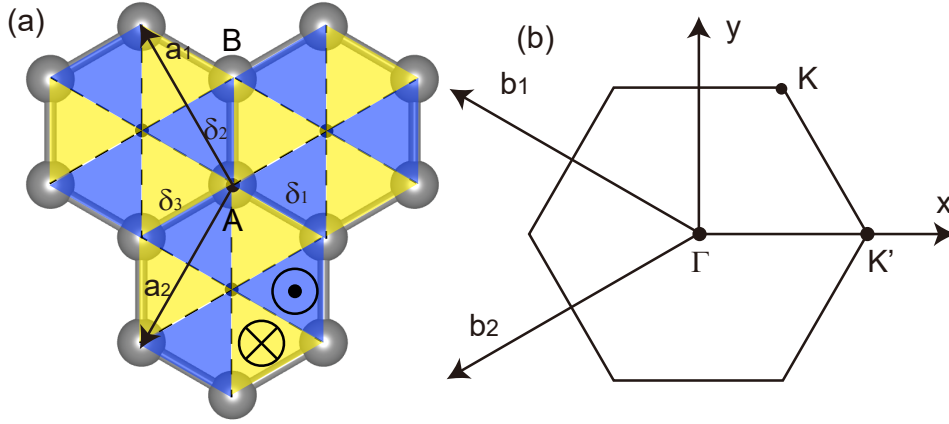


FIG. S5: (color online) (a) Distribution of periodic local magnetic fluxes in hexagonal plaquette of monolayer graphene with sublattices A and B. The blue region (\odot) and yellow region (\otimes) denote outward-to-the-plane and inward-to-the-plane magnetic fluxes, respectively. (b) The monolayer Brillouin Zone.

where we define a complex parameter $\alpha(\varphi) = \alpha_0 e^{i\varphi}$. The chiral symmetric model $H(\mathbf{r})$ ($\varphi = 0$) of conventional TBG can be written as

$$H(\mathbf{r}) = \begin{pmatrix} 0 & D^*(-\mathbf{r}) \\ D(\mathbf{r}) & 0 \end{pmatrix}, D(\mathbf{r}) = \begin{pmatrix} 2\bar{\partial} & \alpha_0 U(\mathbf{r}) \\ \alpha_0 U(-\mathbf{r}) & 2\bar{\partial} \end{pmatrix}. \quad (\text{A8})$$

2. Approximate symmetry in the low energy

The Hamiltonian $H(\mathbf{r})$ of conventional TBG belongs to magnetic point group $6'22'$, including $C_{3z} = e^{i\frac{2\pi}{3}\tau_z}\sigma_0$, $C_{2z}T = \tau_x\sigma_0\mathcal{K}$, $C_{2y} = \tau_y\sigma_y$ and $C_{2x}T = i\tau_z\sigma_y\mathcal{K}$ with sublattice index τ and layer index σ , where T is time reversal operator and \mathcal{K} is the complex conjugation. These symmetries and the moiré translations generate the magnetic space group $P6'2'2$ (No.177.151 in BNS settings). In addition, we can introduce an anti-unitary particle-hole operator $\mathcal{P} = i\tau_x\sigma_y\mathcal{K}$, which satisfies $\mathcal{P}^2 = -1$. It acts on the Hamiltonian $H(\mathbf{r})$ as

$$\mathcal{P}H(\mathbf{r})\mathcal{P}^{-1} = -H(\mathbf{r}). \quad (\text{A9})$$

Furthermore, we define a chiral operator $S = \tau_z\sigma_0$ with $S^2 = 1$. Under chiral symmetry S , the Hamiltonian $H(\mathbf{r})$ transforms as

$$SH(\mathbf{r})S^{-1} = -H(\mathbf{r}). \quad (\text{A10})$$

By combining particle-hole and chiral operators, we can define an effective time reversal operator $\tilde{T} = \tau_y\sigma_y\mathcal{K}$ with $\tilde{T}^2 = 1$. Subsequently, the Hamiltonian $H(\mathbf{r})$ is transformed as follows:

$$\tilde{T}H(\mathbf{r})\tilde{T}^{-1} = H(\mathbf{r}). \quad (\text{A11})$$

Due to effective time reversal operator \tilde{T} , we can also define other crystalline symmetries, including $C_{2z} = i\tau_z\sigma_y$ and $C_{2x} = \tau_x\sigma_0$.

In the presence of the alternating magnetic fluxes, the Hamiltonian $H_{\mathbf{k}}^\varphi(\mathbf{r})$ exhibits a magnetic group $P6'$ (No.168.111 in BNS settings). The corresponding magnetic point group, denoted as $6'$, encompasses symmetries such as $C_{3z} = e^{i\frac{2\pi}{3}\tau_z}\sigma_0$ and $C_{2z}T = \tau_x\sigma_0\mathcal{K}$. Notably, the crystalline symmetries C_{2x} and C_{2y} in conventional TBG are broken due to the introduction of magnetic phase $e^{i\varphi}$. However, the particle-hole operator $\mathcal{P} = i\tau_x\sigma_y\mathcal{K}$, the chiral operator $S = \tau_z\sigma_0$ and the effective time reversal operator $\tilde{T} = \tau_y\sigma_y\mathcal{K}$ are always preserved.

Despite the disruption of crystalline symmetries C_{2x} and C_{2y} induced by the magnetic phase, it is noteworthy that within the low-energy regime, the Hamiltonian $H^\varphi(\mathbf{r})$ approximately retains these symmetries. To prove this, we can define the Hamiltonian difference $\Delta H_{x/y}$ as

$$\Delta H_x = (C_{2x})H^\varphi(\mathbf{r})(C_{2x})^{-1} - H^\varphi(C_{2x}\mathbf{r}), \quad \Delta H_y = (C_{2y})H^\varphi(\mathbf{r})(C_{2y})^{-1} - H^\varphi(C_{2y}\mathbf{r}). \quad (\text{A12})$$

Put $C_{2x} = \tau_x\sigma_0$ and $C_{2y} = \tau_y\sigma_y$ into Eq.A12, and the Hamiltonian difference $\Delta H_{x/y}$ becomes

$$\Delta H_x = 2 \sin \varphi \begin{pmatrix} 0 & 0 & \partial & 0 \\ 0 & 0 & 0 & \partial \\ -\bar{\partial} & 0 & 0 & 0 \\ 0 & -\bar{\partial} & 0 & 0 \end{pmatrix}, \quad \Delta H_y = -2 \sin \varphi \begin{pmatrix} 0 & 0 & \partial & 0 \\ 0 & 0 & 0 & \partial \\ -\bar{\partial} & 0 & 0 & 0 \\ 0 & -\bar{\partial} & 0 & 0 \end{pmatrix}, \quad (\text{A13})$$

where $\varphi \neq \frac{\pi}{2}$. At $\varphi = \frac{\pi}{2}$, the Dirac Hamiltonian for monolayer is from $H_{Dirac} = -v\mathbf{k} \cdot \sigma$ to $H_{Dirac} = -v\mathbf{k} \times \sigma$, and the Hamiltonian $H^\varphi(\mathbf{r})$ has exact rotational symmetries C_{2x} and C_{2y} .

In the momentum lattice, we can arrange the basis as $\hat{\Psi}_{\mathbf{k}} = \sum_{m,n} \oplus (\hat{\psi}_{A;\mathbf{k}+\mathbf{g}_{mn}}^t, \hat{\psi}_{B;\mathbf{k}+\mathbf{g}_{mn}}^t, \hat{\psi}_{A;\mathbf{k}+\mathbf{g}_{mn}+\mathbf{q}_1}^b, \hat{\psi}_{B;\mathbf{k}+\mathbf{g}_{mn}+\mathbf{q}_1}^b)^T$ with \mathbf{g}_{mn} being the lattice of momenta. Then, the the Hamiltonian difference $\Delta H_{x/y}$ can be rewritten as

$$\Delta H_{x/y} = \pm 2 \sin \varphi \sum_{m,n} \oplus \begin{pmatrix} (\mathbf{k}_x + \mathbf{g}_{mn,x})\sigma_x + (\mathbf{k}_y + \mathbf{g}_{mn,y})\sigma_y & 0 \\ 0 & (\mathbf{k}_x + \mathbf{g}_{mn,x} + \mathbf{q}_{1,x})\sigma_x + (\mathbf{k}_y + \mathbf{g}_{mn,y} + \mathbf{q}_{1,y})\sigma_y \end{pmatrix} \quad (\text{A14})$$

Consequently, the Hamiltonian difference $\Delta H_{x/y}$ is proportional to the magnitude of momentum k . In the low energy, the momentum k is exceedingly small, and the $\Delta H_{x/y}$ approximately equal to zero. This implies that within the low-energy spectrum, the symmetries C_{2x} and C_{2y} are effectively retained. In Fig.S6(b) and (c), we present the band structures corresponding to the magnetic phase $\varphi = 0.254\pi$ at magic $\alpha_M = 1.379$ along general lines $\Gamma\beta_1$, $\Gamma\beta_2$ and $\Gamma\beta_3$, where these lines in Fig.S6(a) are interconnected by C_{2x} and C_{2y} symmetries. The general lines $\Gamma\beta_{1,2,3}$ remain consistent in the low-energy spectrum, while there are differences in the high-energy spectrum. Thus, it is evident that within the low-energy spectrum, the Hamiltonian $H^\varphi(\mathbf{r})$ approximately retains C_{2x} and C_{2y} symmetries.

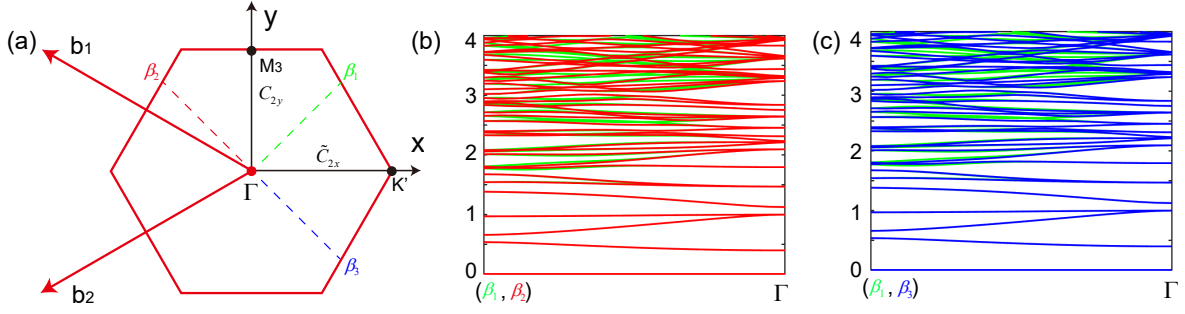


FIG. S6: (color online) (a) Three general lines $\Gamma\beta_1$, $\Gamma\beta_2$ and $\Gamma\beta_3$ in moiré BZ are connected each other by C_{2x} and C_{2y} symmetries. (b) The band structure along $\Gamma\beta_1$ and $\Gamma\beta_2$. (c) The band structure along $\Gamma\beta_1$ and $\Gamma\beta_3$. The green, red and blue label the band structure along $\Gamma\beta_1$, $\Gamma\beta_2$ and $\Gamma\beta_3$, respectively.

3. Symmetry correspondence between momentum space and real space

Here, we discuss the symmetry correspondence between momentum space and real space in the wave function. The four-component wave function can be expressed as $\Psi_{\mathbf{k}}(\mathbf{r}) = (\psi_{\mathbf{k}}^{\top}(\mathbf{r}) \chi_{\mathbf{k}}^{\top}(\mathbf{r}))^{\top}$, where $\psi_{\mathbf{k}}^{\top}(\mathbf{r})$ and $\chi_{\mathbf{k}}^{\top}(\mathbf{r})$ denote the two component wave function. By acting $C_{2z}T$ symmetry on the wave function $\Psi_{\mathbf{k}}(\mathbf{r})$, we obtain the following result:

$$C_{2z}T \begin{pmatrix} \psi_{\mathbf{k}}(\mathbf{r}) \\ \chi_{\mathbf{k}}(\mathbf{r}) \end{pmatrix} = \begin{pmatrix} \chi_{\mathbf{k}}^*(\mathbf{r}) \\ \psi_{\mathbf{k}}^*(\mathbf{r}) \end{pmatrix} = \begin{pmatrix} \psi_{\mathbf{k}}(-\mathbf{r}) \\ \chi_{\mathbf{k}}(-\mathbf{r}) \end{pmatrix}. \quad (\text{A15})$$

Hence, $\chi_{\mathbf{k}}(\mathbf{r}) = \psi_{\mathbf{k}}^*(-\mathbf{r})$, and the wave function can be rewritten as $\Psi_{\mathbf{k}}(\mathbf{r}) = (\psi_{\mathbf{k}}^{\top}(\mathbf{r}) \psi_{\mathbf{k}}^{\dagger}(-\mathbf{r}))^{\top}$. Due to C_{2x} symmetry, the wave function $\Psi_{\mathbf{k}}(\mathbf{r})$ becomes

$$C_{2x} \begin{pmatrix} \psi_{\mathbf{k}}(\mathbf{r}) \\ \psi_{\mathbf{k}}^*(-\mathbf{r}) \end{pmatrix} = \begin{pmatrix} \psi_{\mathbf{k}}^*(-\mathbf{r}) \\ \psi_{\mathbf{k}}(\mathbf{r}) \end{pmatrix} = \begin{pmatrix} \psi_{C_{2x}\mathbf{k}}(C_{2x}\mathbf{r}) \\ \psi_{C_{2x}\mathbf{k}}^*(-C_{2x}\mathbf{r}) \end{pmatrix}, \quad (\text{A16})$$

Then, $\psi_{\mathbf{k}}(\mathbf{r}) = \psi_{C_{2x}\mathbf{k}}^*(-C_{2x}\mathbf{r})$. Hence, the C_{2x} symmetry in momentum space corresponds to C_{2y}^r symmetry in real space, indicating that the norm of wave function $\psi_{\mathbf{k}}(\mathbf{r})$ on the C_{2x} -symmetric \mathbf{k} path exhibits C_{2y}^r symmetry in real space. Similarly, the norm of wave function $\psi_{\mathbf{k}}(\mathbf{r})$ on the C_{2y} -symmetric \mathbf{k} path displays C_{2x}^r symmetry in real space.

4. Topological property

Here, we explore the topological properties for quadruple flat bands. Fig.S7 (b) illustrates Wilson loop $W(\mathbf{k}_x)$ corresponding to the quadruple flat bands, highlighted by the green dotted box in Fig.S7 (a), where we perform an integration procedure along the \mathbf{b}_{\parallel} direction and present the resulting spectra along the \mathbf{b}_{\perp} direction. The partner switch in the Wannier centers from $\mathbf{k} = -\mathbf{b}_{\perp}/2$ to $\mathbf{k} = 0$ indicates that quadruple flat bands possess a nontrivial topology $\mathbb{Z}_2 = 1$, consistent with the argument in Ref.[2]. Furthermore, by introducing a staggered potential term $V\sigma_z$ on both layers, the Dirac points at K and K' can be gapped while the two degeneracy at Γ in Fig.S7 (e) will always be maintained. Under the effect of the staggered potential, the quadruple flat bands will split into two double flat bands in Fig.S7 (c), and Fig.S7 (d) shows Wilson loop $W(\mathbf{k}_x)$ of occupied double flat bands, indicating that the occupied double flat bands have Chern number $C = +1$. To investigate the topological properties of every flat band, we add an C_3 -breaking term $V'\sigma_x$ to the interlayer coupling along \mathbf{q}_1 direction, which can gap the Dirac points and two degeneracy at Γ . Fig.S7 (f) show the corresponding band structure with $V' = 0.2$ at magic value $\alpha_M = 1.379e^{i\varphi_N}$, where the quadruple flat bands split into four non-degenerate bands. By calculating the Chern number, band No.2/3 originating from Dirac point possess $C_2 = +1$ and $C_3 = -1$, while the Chern number of band No.1/4 from band inversion vanish, as shown in Fig.S7 (f).

5. Condition for the emergence of multi-fold degenerate flat bands

In the main text, we have presented the conditions for the emergence of multi-fold degenerate flat bands, which are twice the degeneracy of magic angles. We will provide a rigorous proof of this assertion, and the eigenfunction of the Hamiltonian $H^{\varphi}(\mathbf{r})$

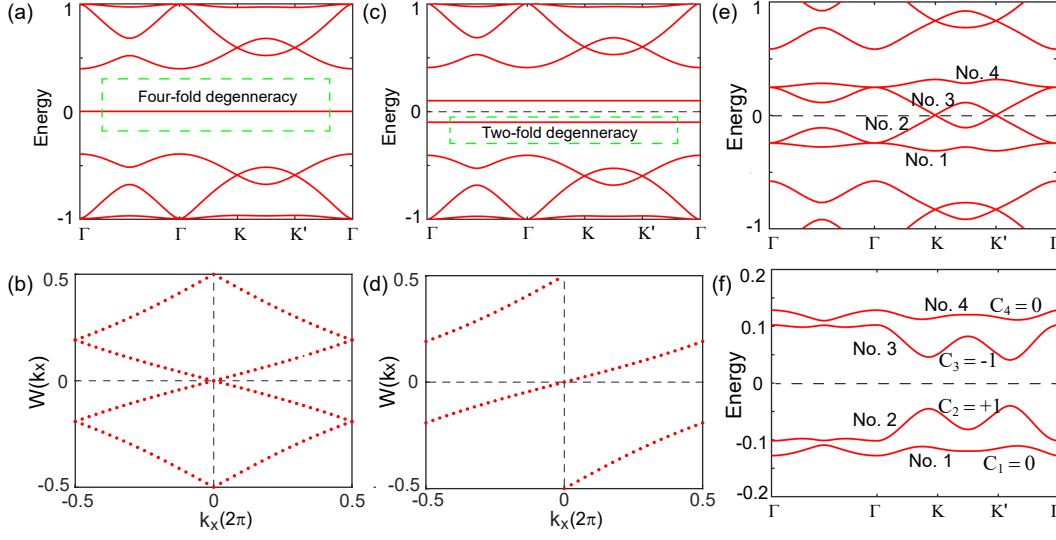


FIG. S7: (color online) (a) and (b) Band structures and Wilson loops $W(\mathbf{k}_x)$ of quadruple flat bands at magic value $\alpha_M = 1.379e^{i\varphi_N}$ with magnetic phase $\varphi_N = 0.254\pi$. (c) and (d) Band structures with $V = 0.1$ and Wilson loops $W(\mathbf{k}_x)$ of occupied double flat bands at magic value $\alpha_M = 1.379e^{i\varphi_N}$ with magnetic phase $\varphi_N = 0.254\pi$. (e) and (f) Band structures at $\alpha_M = 1.0e^{i\varphi_N}$ and at magic value $\alpha_M = 1.379e^{i\varphi_N}$ with $V' = 0.2$. The green dotted boxes in (a) and (b) highlighted quadruple flat bands and occupied double flat bands. Momentum \mathbf{k}_x is along \mathbf{b}_1 direction.

can be written as

$$\begin{pmatrix} 0 & D_{\mathbf{k}}^{\varphi*}(-\mathbf{r}) \\ D_{\mathbf{k}}^{\varphi}(\mathbf{r}) & 0 \end{pmatrix} \begin{pmatrix} \psi_{\mathbf{k}}^n(\mathbf{r}) \\ \chi_{\mathbf{k}}^n(\mathbf{r}) \end{pmatrix} = E_{\mathbf{k}} \begin{pmatrix} \psi_{\mathbf{k}}^n(\mathbf{r}) \\ \chi_{\mathbf{k}}^n(\mathbf{r}) \end{pmatrix}, \quad (\text{A17})$$

where $\psi_{\mathbf{k}}^n(\mathbf{r})$ and $\chi_{\mathbf{k}}^n(\mathbf{r})$ are two component wave functions with n -fold degeneracy. For zero energy flat bands ($E_{\mathbf{k}} = 0$), the eigenfunction Eq.A17 becomes

$$D_{\mathbf{k}}^{\varphi}(\mathbf{r})\psi_{\mathbf{k}}^n(\mathbf{r}) = 0, \quad D_{\mathbf{k}}^{\varphi*}(-\mathbf{r})\chi_{\mathbf{k}}^n(\mathbf{r}) = 0. \quad (\text{A18})$$

Then, the zero energy eigenstates can be written as

$$\Psi_{\mathbf{k},1}^n(\mathbf{r}) = \begin{pmatrix} \psi_{\mathbf{k}}^n(\mathbf{r}) \\ 0 \end{pmatrix}, \quad \Psi_{\mathbf{k},2}^n(\mathbf{r}) = \begin{pmatrix} 0 \\ \chi_{\mathbf{k}}^n(\mathbf{r}) \end{pmatrix}. \quad (\text{A19})$$

Due to $\chi_{\mathbf{k}}^n(\mathbf{r}) = \psi_{\mathbf{k}}^{n*}(-\mathbf{r})$, the eigenstates Eq.A19 become

$$\Psi_{\mathbf{k},1}^n(\mathbf{r}) = \begin{pmatrix} \psi_{\mathbf{k}}^n(\mathbf{r}) \\ 0 \end{pmatrix}, \quad \Psi_{\mathbf{k},2}^n(\mathbf{r}) = \begin{pmatrix} 0 \\ \psi_{\mathbf{k}}^{n*}(-\mathbf{r}) \end{pmatrix}. \quad (\text{A20})$$

The relation between $D_{\mathbf{k}}^{\varphi}(\mathbf{r})$ and $T_{\mathbf{k}}$ reads

$$D_{\mathbf{k}}^{\varphi}(\mathbf{r}) = (2\bar{\partial} - \mathbf{k})(I - \alpha(\varphi)T_{\mathbf{k}}). \quad (\text{A21})$$

If $T_{\mathbf{k}}$ has eigenvalue $\frac{1}{\alpha(\varphi)}$ independent of \mathbf{k} , the eigenfunction reads

$$T_{\mathbf{k}}\phi_{\mathbf{k}}^n(\mathbf{r}) = \frac{1}{\alpha(\varphi)}\phi_{\mathbf{k}}^n(\mathbf{r}), \quad (\text{A22})$$

where $\phi_{\mathbf{k}}^n(\mathbf{r})$ are eigenvectors of $T_{\mathbf{k}}$ with n -fold degeneracy. Then, the eigenfunction of $D_{\mathbf{k}}^{\varphi}(\mathbf{r})$ can be written as

$$D_{\mathbf{k}}^{\varphi}(\mathbf{r})\phi_{\mathbf{k}}^n(\mathbf{r}) = (2\bar{\partial} - \mathbf{k})(I - \alpha(\varphi)T_{\mathbf{k}})\phi_{\mathbf{k}}^n(\mathbf{r}) = 0, \quad (\text{A23})$$

indicating that $\psi_{\mathbf{k}}^n(\mathbf{r}) = \phi_{\mathbf{k}}^n(\mathbf{r})$ are eigenvectors of $D_{\mathbf{k}}^{\varphi}(\mathbf{r})$ with n -fold degeneracy. Hence, based on Eq.A20, the degeneracy of flat bands are twice the degeneracy of real eigenvalues.

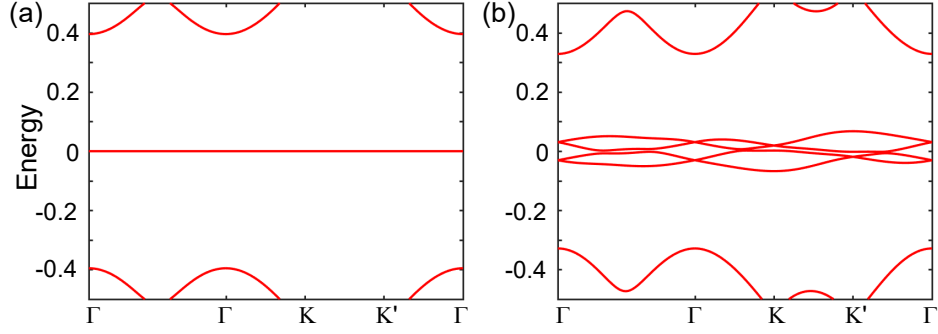


FIG. S8: (color online) The band structures at magic value $\alpha_M = 1.379e^{i\varphi_N}$ with magnetic phase $\varphi_N = 0.254\pi$ in the absence and presence of intra-sublattice interlayer coupling: (a) $\omega_{AA} = 0$, (b) $\omega_{AA}/\omega_{AB} = 0.15$. The symbols ω_{AA} and ω_{AB} represent the intra-sublattice and inter-sublattice interlayer couplings, respectively.

6. Effect of the intra-sublattice interlayer coupling

Here, we discuss the effect of the intra-sublattice interlayer coupling on the absolutely flat bands. Usually, the area of the AA stacking region undergoes a reduction due to lattice relaxation effects, and the absolutely flat bands can be obtained at magic angle when the intra-sublattice interlayer coupling ω_{AA} vanishes[1]. Then, we take the magic value $\alpha_M = 1.379e^{i\varphi_N}$ as an example with magnetic phase $\varphi_N = 0.254\pi$, Fig.S8(a) shows the the absolutely flat bands with four-fold degeneracy in the absence of intra-sublattice interlayer coupling. However, when ω_{AA} is switched on, the absolutely flat bands exhibit a slight dispersion, as shown in Fig.S8 (b).

Appendix B: Theta function and flat band wave function

In this section, we introduce the definitions of the theta function and delve into its inherent properties. Subsequently, we utilize these properties of the theta function to derive analytical expressions for the flat band wave function. Furthermore, we investigate the nodal evolution of flat band wave function in real space.

1. Theta function

The theta function[3] can be defined as

$$\vartheta(z|\tau) = \sum_{n=-\infty}^{\infty} e^{\pi i \tau n^2 + 2\pi i n z} \quad (\text{B1})$$

Where $n \in \mathbb{Z}$, τ are complex parameters with $\text{Im}(\tau) > 0$, and z is complex variable. It can be checked that

$$\vartheta(z+1|\tau) = \sum_{n=-\infty}^{+\infty} e^{\pi i \tau n^2 + 2\pi i n(z+1)} = \sum_{n=-\infty}^{+\infty} e^{\pi i \tau n^2 + 2\pi i n z} = \vartheta(z|\tau), \quad (\text{B2})$$

$$\vartheta(z+\tau|\tau) = \sum_{n=-\infty}^{+\infty} e^{\pi i \tau n^2 + 2\pi i n(z+\tau)} = e^{-\pi i \tau - 2\pi i z} \sum_{n=-\infty}^{+\infty} e^{\pi i (n+1)^2 \tau + 2\pi i (n+1)z} = e^{-\pi i \tau - 2\pi i z} \vartheta(z|\tau), \quad (\text{B3})$$

$$\vartheta(-z|\tau) = \sum_{n=-\infty}^{\infty} e^{\pi i \tau n^2 - 2\pi i n z} = \sum_{n=-\infty}^{\infty} e^{\pi i \tau (-n)^2 + 2\pi i (-n)z} = \vartheta(z|\tau) \quad (\text{B4})$$

All zeros of the theta functions are simple zeros and are given as

$$\vartheta(z|\tau) = 0 \iff z = m + n\tau + \frac{1}{2} + \frac{\tau}{2}, \quad m, n \in \mathbb{Z}. \quad (\text{B5})$$

The theta functions with rational characteristics a and b are defined as

$$\vartheta_{a,b}(z|\tau) = \sum_{n=-\infty}^{+\infty} e^{i\pi\tau(n+a)^2} e^{2i\pi(n+a)(z+b)}, \quad (\text{B6})$$

where τ are complex parameters with $\text{Im}(\tau) > 0$, and the range of a is $[0,1]$. z is complex variables. The relation between $\vartheta_{a,b}(z|\tau)$ and $\vartheta(z|\tau)$ is

$$\vartheta_{a,b}(z|\tau) = e^{\pi i a^2 \tau + 2\pi i a(z+b)} \vartheta(z+a\tau+b|\tau). \quad (\text{B7})$$

Then, it can be checked that

$$\vartheta_{a,b}(z+1|\tau) = e^{2i\pi a} \vartheta_{a,b}(z|\tau), \vartheta_{a\pm 1,b}(z|\tau) = \vartheta_{a,b}(z|\tau), \vartheta_{a,b}(z+\tau|\tau) = e^{-2i\pi(z+b+\frac{\tau}{2})} \vartheta_{a,b}(z|\tau) m, \quad (\text{B8})$$

The simple zeros are

$$\vartheta_{a,b}(z|\tau) = 0 \leftrightarrow z = \frac{1+\tau}{2} - (a\tau+b) + (m\tau+n), \quad m, n \in \mathbb{Z}, \quad (\text{B9})$$

2. Wave function for quadruple flat bands

Here, we turn to construct wave functions for flat bands No.1/2, and the wave functions for flat bands No.3/4 can be generated by chiral symmetry. As discussed regarding the nodal characteristics of wave function at \mathbf{K} point in the main text, the flat band No.1 exhibit two nodes at the AA and BA stackings with linear real-space dependence, while the flat band No.2 features a single node at the AB stacking with real-space quadratic dependence. Based on these nodal features, the analytical expressions for flat band wave functions can be constructed as

$$\Psi_{\mathbf{K},i}(\mathbf{r}) = f_{\mathbf{k}}(z) \Psi_{\mathbf{K},i}(\mathbf{r}), \quad f_{\mathbf{k}}(z) = \frac{\vartheta_{a,b}(\frac{z}{L_1} | \frac{L_2}{L_1}) \vartheta_{a',b'}(\frac{z}{L_1} | \frac{L_2}{L_1})}{\vartheta_{e,f}(\frac{z}{L_1} | \frac{L_2}{L_1}) \vartheta_{e',f'}(\frac{z}{L_1} | \frac{L_2}{L_1})}, \quad (\text{B10})$$

where $i = 1, 2$ is band index, and the origin of \mathbf{k} is chosen at Γ in the moiré BZ. The parameters a/a' and b/b' are functions of \mathbf{k} , while e/e' and f/f' are determined by nodal points of wave functions $\Psi_{\mathbf{K},i}(\mathbf{r})$. If the two nodal points of $\Psi_{\mathbf{K},i}(\mathbf{r})$ are located at $c_1\mathbf{L}_I + c_{II}\mathbf{L}_{II}$ and $c'_1\mathbf{L}_I + c'_{II}\mathbf{L}_{II}$ in the moiré unit cell, by using Eq.B9, the parameters e/e' and f/f' can be expressed as

$$e = \frac{1}{2} - c_{II}, f = \frac{1}{2} - c_I, e' = \frac{1}{2} - c'_{II}, f' = \frac{1}{2} - c'_I \quad (\text{B11})$$

According to Bloch theorem, $H_{\mathbf{k}}^\varphi(\mathbf{r} + \mathbf{L}_{I/II}) = UH_{\mathbf{k}}^\varphi(\mathbf{r})U^{-1}$ with $U = \text{diag}(e^{-i2\pi/3}, e^{i2\pi/3})$, the wave functions $\Psi_{\mathbf{k},i}(\mathbf{r})$ shall obey the Bloch boundary condition

$$\Psi_{\mathbf{k},i}(\mathbf{r} + \mathbf{L}_{I/II}) = e^{i\mathbf{k}\cdot\mathbf{L}_{I/II}}U\Psi_{\mathbf{k},i}(\mathbf{r}). \quad (\text{B12})$$

Putting Eq.B10 into Eq.B12, $f_{\mathbf{k}}(z)$ also satisfies Bloch boundary condition

$$f_{\mathbf{k}}(z + \mathbf{L}_{I/II}) = e^{i(\mathbf{k}-\mathbf{K})\cdot\mathbf{L}_{I/II}}f_{\mathbf{k}}(z). \quad (\text{B13})$$

Then, by using $\vartheta_{a,b}(z + 1|\tau) = e^{2i\pi a}\vartheta_{a,b}(z|\tau)$ and $\vartheta_{a,b}(z + \tau|\tau) = e^{-2i\pi(z+b+\frac{\tau}{2})}$ in the Eq.B8, we can get

$$e^{2i\pi(a+a'-e-e')} = e^{i(\mathbf{k}-\mathbf{K})\cdot\mathbf{L}_I}, \quad e^{-2i\pi(b+b'-f-f')} = e^{i(\mathbf{k}-\mathbf{K})\cdot\mathbf{L}_{II}}. \quad (\text{B14})$$

Therefore,

$$a + a' = e + e' + \frac{(\mathbf{k} - \mathbf{K}) \cdot \mathbf{L}_I}{2\pi}, \quad b + b' = f + f' - \frac{(\mathbf{k} - \mathbf{K}) \cdot \mathbf{L}_{II}}{2\pi}. \quad (\text{B15})$$

By denoting the two nodal positions of $\Psi_{\mathbf{k},i}(\mathbf{r})$ as $l\mathbf{L}_I + m\mathbf{L}_{II}$ and $l'\mathbf{L}_I + m'\mathbf{L}_{II}$, abbreviated as (l, m) and (l', m') , the relationship between nodal coordinates and rational characteristics can be expressed as

$$l = \frac{1}{2} - b, l' = \frac{1}{2} - b', m = \frac{1}{2} - a, m' = \frac{1}{2} - a'. \quad (\text{B16})$$

Combined with Eq.B15, the relationship between nodal coordinates reads

$$m + m' = 1 - e - e' - \frac{(\mathbf{k} - \mathbf{K}) \cdot \mathbf{L}_I}{2\pi}, \quad l + l' = 1 - f - f' + \frac{(\mathbf{k} - \mathbf{K}) \cdot \mathbf{L}_{II}}{2\pi}. \quad (\text{B17})$$

For flat band No.1, the two nodal points of $\Psi_{\mathbf{K},1}(\mathbf{r})$ are located at AA and BA stacking points with $\mathbf{r}_{AA} = 0$ and $\mathbf{r}_{BA} = \frac{-2\mathbf{L}_I - \mathbf{L}_{II}}{3}$, and we can get

$$e = \frac{1}{2}, \quad f = \frac{1}{2}, \quad e' = \frac{5}{6}, \quad f' = \frac{7}{6}. \quad (\text{B18})$$

Hence, the wave function $\Psi_{\mathbf{k},1}(\mathbf{r})$ for flat band No.1 and the relationship between nodal coordinates and rational characteristics are given by

$$\Psi_{\mathbf{k},1}(\mathbf{r}) = \frac{\vartheta_{a_1, b_1}(\frac{z}{L_1} | \frac{L_2}{L_1}) \vartheta_{a'_1, b'_1}(\frac{z}{L_1} | \frac{L_2}{L_1})}{\vartheta_{\frac{1}{2}, \frac{1}{2}}(\frac{z}{L_1} | \frac{L_2}{L_1}) \vartheta_{\frac{5}{6}, \frac{7}{6}}(\frac{z}{L_1} | \frac{L_2}{L_1})} \Psi_{\mathbf{K},1}(\mathbf{r}), \quad (\text{B19})$$

$$a_1 + a'_1 = \frac{4}{3} + \frac{(\mathbf{k} - \mathbf{K}) \cdot \mathbf{L}_I}{2\pi}, \quad b_1 + b'_1 = \frac{5}{3} - \frac{(\mathbf{k} - \mathbf{K}) \cdot \mathbf{L}_{II}}{2\pi}. \quad (\text{B20})$$

The corresponding relationship between nodal coordinates is

$$l_1 + l'_1 = -\frac{2}{3} + \frac{(\mathbf{k} - \mathbf{K}) \cdot \mathbf{L}_{II}}{2\pi}, \quad m_1 + m'_1 = -\frac{1}{3} - \frac{(\mathbf{k} - \mathbf{K}) \cdot \mathbf{L}_I}{2\pi}. \quad (\text{B21})$$

For flat band No.2, the nodal point of $\psi_{\mathbf{K},2}(\mathbf{r})$ is located at AB stacking point with $\mathbf{r}_{AB} = \frac{-\mathbf{L}_I + \mathbf{L}_{II}}{3}$

$$e = \frac{1}{6}, \quad f = \frac{5}{6}, \quad e' = \frac{1}{6}, \quad f' = \frac{5}{6} \quad (\text{B22})$$

Hence, the wave function $\Psi_{\mathbf{k},2}(\mathbf{r})$ for flat band No.2 and relationship between nodal coordinates and rational characteristics can be expressed as

$$\Psi_{\mathbf{k},2}(\mathbf{r}) = \frac{\vartheta_{a_2,b_2}\left(\frac{z}{L_1} \middle| \frac{L_2}{L_1}\right) \vartheta_{a'_2,b'_2}\left(\frac{z}{L_1} \middle| \frac{L_2}{L_1}\right)}{[\vartheta_{\frac{1}{6},\frac{5}{6}}\left(\frac{z}{L_1} \middle| \frac{L_2}{L_1}\right)]^2} \Psi_{\mathbf{K},2}(\mathbf{r}), \quad (\text{B23})$$

$$a_2 + a'_2 = \frac{1}{3} + \frac{(\mathbf{k} - \mathbf{K}) \cdot \mathbf{L}_I}{2\pi}, \quad b_2 + b'_2 = \frac{5}{3} - \frac{(\mathbf{k} - \mathbf{K}) \cdot \mathbf{L}_I}{2\pi}, \quad (\text{B24})$$

The corresponding relationship between nodal coordinates is

$$l_2 + l'_2 = -\frac{2}{3} + \frac{(\mathbf{k} - \mathbf{K}) \cdot \mathbf{L}_I}{2\pi}, \quad m_2 + m'_2 = \frac{2}{3} - \frac{(\mathbf{k} - \mathbf{K}) \cdot \mathbf{L}_I}{2\pi}. \quad (\text{B25})$$

Due to moiré lattice translation symmetry, the nodal positions of wave function $\Psi_{\mathbf{K},i}(\mathbf{r})$ can be increased by any integer multiple of the translation vectors $\mathbf{L}_{I/II}$. Hence, Eq.B20 and Eq.B24 can be written in uniform form with arbitrary integers n_I and n_{II}

$$a_i + a'_i = \frac{1}{3} + \frac{(\mathbf{k} - \mathbf{K}) \cdot \mathbf{L}_I}{2\pi} + n_I, \quad b_i + b'_i = \frac{2}{3} - \frac{(\mathbf{k} - \mathbf{K}) \cdot \mathbf{L}_I}{2\pi} + n_{II}. \quad (\text{B26})$$

Then, the uniform relationship between nodal coordinates is

$$l_i + l'_i = \frac{1}{3} + \frac{(\mathbf{k} - \mathbf{K}) \cdot \mathbf{L}_I}{2\pi} + n_{II}, \quad m_i + m'_i = \frac{2}{3} - \frac{(\mathbf{k} - \mathbf{K}) \cdot \mathbf{L}_I}{2\pi} + n_I. \quad (\text{B27})$$

3. Nodal evolution in real space

Here, we discuss the nodal evolution and flat band wave function in the moiré BZ. As the momentum \mathbf{k} varies, the nodal points for the FBs move in real space and their coordinates obey Eq.B27. We take three representative paths $\mathbf{M}_1\mathbf{M}_3$, $\mathbf{M}_3\mathbf{M}'_3$ (C_{2y} -symmetric) and $\mathbf{M}'_3\mathbf{K}$ (C_{2x} -symmetric) to show how nodal points evolve in the moiré unit cell, which is denoted by circles with blue-green-yellow-red gradient color in Fig.S9(a). The corresponding evolution of nodes for bands No.1, 2 in the moiré unit cell is displayed in Fig.S9 (b) and (c). As previously discussed, the norm of WFs $\psi_{\mathbf{k}}(\mathbf{r})$ on the C_{2y} -symmetric $\mathbf{M}_3\mathbf{M}'_3$ path and C_{2x} -symmetric $\mathbf{M}'_3\mathbf{K}$ path preserves C_{2x}^r and C_{2y}^r symmetries in the real space, respectively. When \mathbf{k} is located at \mathbf{M}_1 point, the FB WF $\psi_{\mathbf{k},1}$ ($\psi_{\mathbf{k},2}$) has two nodal points at AA (X'_3) and X_2 (X_1). As \mathbf{k} varies from \mathbf{M}_1 to \mathbf{M}_3 , for $\psi_{\mathbf{k},1}$ one nodal point moves continuously from X_2 to X_1 , while the other first moves away from AA and then returns. Correspondingly, two nodal points of the $\psi_{\mathbf{k},2}$ move to X_2 and X_3 . It is apparent that the nodes of both bands are C_{2x}^r -symmetric at \mathbf{M}_3 . With \mathbf{k} further varying along the C_{2y} -symmetric $\mathbf{M}_3\mathbf{M}'_3$ path, both nodes of $\psi_{\mathbf{k},1}$ move along the X_1 -AA lines, and nodes of $\psi_{\mathbf{k},2}$ move from X_2/X_3 to X'_3/X'_2 , preserving C_{2x}^r symmetry. Finally, as \mathbf{k} varies along the C_{2x} -symmetric $\mathbf{M}'_3\mathbf{K}$ path, one nodal point of $\psi_{\mathbf{k},1}$ moves along X'_1 -BA₁ line and the other first moves away from AA along AA-BA₃ line and then returns. In contrast, both nodes of the $\psi_{\mathbf{k},2}$ move towards the AB stacking point and merge to form a second-order node at \mathbf{K} , consistent with our previous analysis. In addition, to confirm the validity of wave function analytical expressions, we calculate the flat-band wave functions from Hamiltonian $H^\varphi(\mathbf{r})$ and Eq.B19/B23 at $\mathbf{k} = \mathbf{M}_3$, which are labelled in red squares and blue triangles in Fig.S9 (d) and (e), and the good agreement between them verifies the validity of wave function from analytical expressions. In the following, we take $\mathbf{K} = \frac{1}{3}\mathbf{b}_I - \frac{2}{3}\mathbf{b}_{II}$, $\mathbf{M}_3 = \frac{1}{2}\mathbf{b}_I - \frac{1}{2}\mathbf{b}_{II}$ and $\mathbf{P} = 0.5\mathbf{b}_I - 0.3\mathbf{b}_{II}$ points as examples to check Eq.B27.

(1) At $\mathbf{k} = \mathbf{K}$, the Eq.B27 becomes

$$l_i + l'_i = \frac{1}{3} + \frac{(\mathbf{K} - \mathbf{K}) \cdot \mathbf{L}_I}{2\pi} + n_{II} = \frac{1}{3} + n_{II}, \quad m_i + m'_i = \frac{2}{3} - \frac{(\mathbf{K} - \mathbf{K}) \cdot \mathbf{L}_I}{2\pi} + n_I = \frac{2}{3} + n_I. \quad (\text{B28})$$

Since the two nodal positions of $\Psi_{\mathbf{K},1}(\mathbf{r})$ are located at AA and BA points with $\mathbf{r}_{AA} = 0$ and $\mathbf{r}_{BA} = \frac{\mathbf{L}_I + 2\mathbf{L}_{II}}{3}$, and the nodal position of $\Psi_{\mathbf{K},2}(\mathbf{r})$ is located at AB point with $\mathbf{r}_{AB} = \frac{-\mathbf{L}_I + \mathbf{L}_{II}}{3}$. Then, we can get

$$l_1 = 0, \quad m_1 = 0, \quad l'_1 = \frac{1}{3}, \quad m'_1 = \frac{2}{3} \quad \text{and} \quad l_2 = -\frac{1}{3}, \quad m_2 = \frac{1}{3}, \quad l'_2 = -\frac{1}{3}, \quad m'_2 = \frac{1}{3}, \quad (\text{B29})$$

which satisfy Eq.B28 with $n_I = n_{II} = 0$ for flat band No.1, and with $n_I = -1$ and $n_{II} = 0$ for flat band No.2.

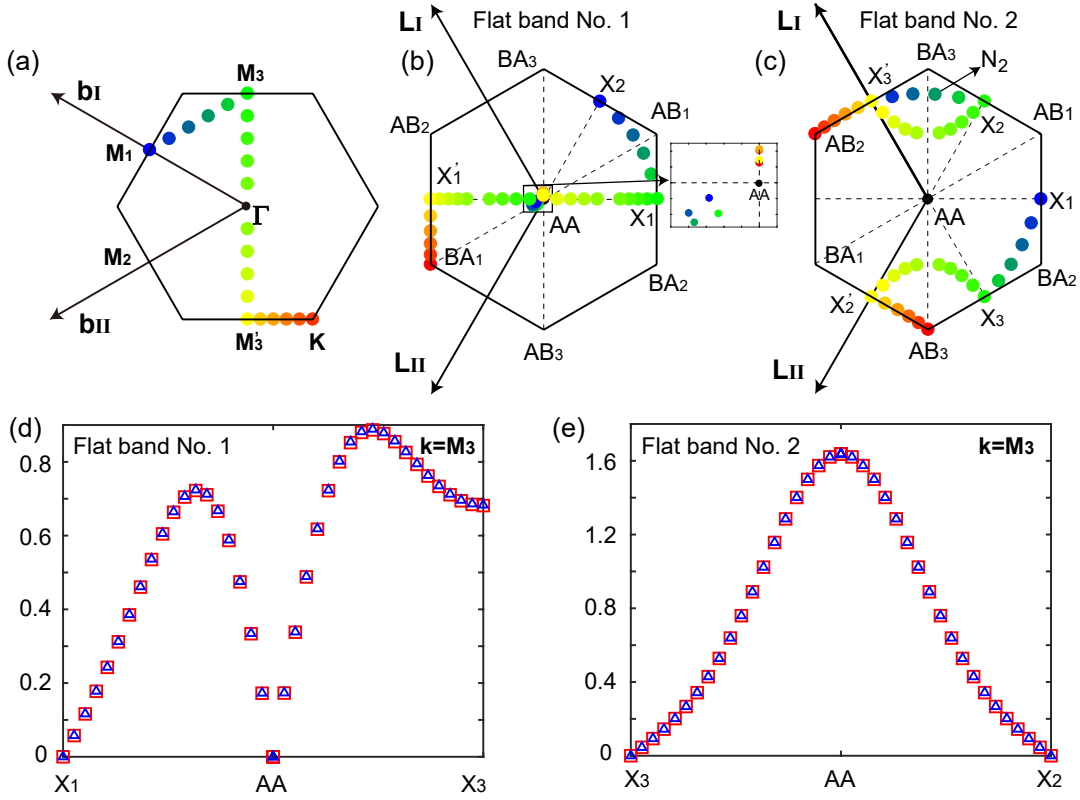


FIG. S9: (color online) (a)-(c) Momentum points at three paths M_1M_3 , $M_3M'_3$ and M'_3K , and a high point $M_3 = 0.5\mathbf{b}_1 - 0.5\mathbf{b}_2$. (b) and (c) Wave function nodal points for FBs No. 1/2 in moiré unit cell indicated by corresponding colors in (a). (d) and (e) The absolute value of wave functions $|\Psi_{\mathbf{k},1/2}(\mathbf{r})|$ for flat bands No.1/2 in moiré unit cell at $\mathbf{k} = M_3$, and the wave functions from Hamiltonian $H^\varphi(\mathbf{r})$ and Eq.B19/B23 are labelled in red squares and blue triangles.

(2) At $\mathbf{k} = M_3$, the Eq.B27 becomes

$$l_i + l'_i = \frac{1}{3} + \frac{(M_3 - K) \cdot L_{II}}{2\pi} + n_{II} = \frac{1}{2} + n_{II}, \quad m_i + m'_i = \frac{2}{3} - \frac{(M_3 - K) \cdot L_I}{2\pi} + n_I = \frac{1}{2} + n_I. \quad (\text{B30})$$

Because the two nodal positions of $\Psi_{M_3,1}(\mathbf{r})$ ($\Psi_{M_3,2}(\mathbf{r})$) are located at $AA(X_2)$ and $X_1(X_3)$ points with $\mathbf{r}_{AA} = 0$ ($\mathbf{r}_{X_2} = \frac{L_{II}}{2}$) and $\mathbf{r}_{X_1} = \frac{L_I + L_{II}}{2}$ ($\mathbf{r}_{X_3} = \frac{L_I}{2}$), then

$$l_1 = 0, \quad m_1 = 0, \quad l'_1 = \frac{1}{2}, \quad m'_1 = \frac{1}{2} \quad \text{and} \quad l_2 = 0, \quad m_2 = \frac{1}{2}, \quad l'_2 = \frac{1}{2}, \quad m'_2 = 0, \quad (\text{B31})$$

which satisfy Eq.B30 with $n_I = n_{II} = 0$ for flat band No.1/2.

(3) At $\mathbf{k} = P$, the Eq.B27 becomes

$$l_i + l'_i = \frac{1}{3} + \frac{(P - K) \cdot L_{II}}{2\pi} + n_{II} = 0.7 + n_{II}, \quad m_i + m'_i = \frac{2}{3} - \frac{(P - K) \cdot L_I}{2\pi} + n_I = 0.5 + n_I. \quad (\text{B32})$$

Since the nodal points of wave functions for flat bands No.1/2 are $N_1 = -0.3265L_1 - 0.5607L_2$, $N'_1 = 0.0266L_1 + 0.0612L_2$, $N_2 = 0.236L_1 - 0.2986L_2$ and $N'_2 = -0.5358L_1 - 0.201L_2$, then we can get

$$l_1 = -0.3265, \quad m_1 = -0.5607, \quad l'_1 = 0.0266, \quad m'_1 = 0.0612 \quad \text{and} \quad l_2 = 0.236, \quad m_2 = -0.2986, \quad l'_2 = -0.5358, \quad m'_2 = -0.201 \quad (\text{B33})$$

which satisfy Eq.B32 with $n_I = n_{II} = -1$ for flat band No.1/2.

Appendix C: Ground states of TBG with alternative magnetic fluxes at half-filling

1. Projected interaction and ground states

Here, we begin with the general Coulomb interaction that describes TBG, and proceed to derive the projected interaction within the flat band basis. By utilizing this projected interaction, we deduce the intrasublattice-intraorbital interaction characterized by chiral symmetry, and its ground states with zero energy can be obtained at half-filling.

a. Projected interaction

The general Hamiltonian describing the Coulomb interaction in TBG can be expressed as

$$\hat{\mathcal{H}}_I = \sum_{\tau, \sigma, \tau', \sigma'}^{i, \delta} V_\delta c_{i, \tau, \sigma}^\dagger c_{i, \tau, \sigma} c_{i+\delta, \tau', \sigma'}^\dagger c_{i+\delta, \tau', \sigma'}, \quad (\text{C1})$$

where $c_{i, \tau, \sigma}$ and $c_{i+\delta, \tau, \sigma}$ denote the annihilation operators for electrons in sublattice τ and layer σ at unit cells i and $i + \delta$, respectively. The parameter V_δ represents the strength of Coulomb interaction between two electrons separated by the vector δ . Considering the small magnitude of the twisted angle, we neglect the dependence of the Hamiltonian on this angle. By performing a Fourier transformation, the interaction Hamiltonian $\hat{\mathcal{H}}_I$ can be written in terms of momentum space as follows:

$$\begin{aligned} \hat{\mathcal{H}}_I &= \sum_{\tau, \sigma, \tau', \sigma'}^{i, \delta} V_\delta c_{i, \tau, \sigma}^\dagger c_{i, \tau, \sigma} c_{i+\delta, \tau', \sigma'}^\dagger c_{i+\delta, \tau', \sigma'}, \\ &= \frac{1}{N^2} \sum_{\tau, \sigma, \tau', \sigma'}^{i, \delta} V_\delta e^{i(\mathbf{k}_1 - \mathbf{k}_2 + \mathbf{k}_3 - \mathbf{k}_4) \cdot \mathbf{R}_i} c_{\mathbf{k}_1, \tau, \sigma}^\dagger c_{\mathbf{k}_2, \tau, \sigma} c_{\mathbf{k}_3, \tau', \sigma'}^\dagger c_{\mathbf{k}_4, \tau', \sigma'} e^{-i\mathbf{k}_3 \cdot \delta} e^{i\mathbf{k}_4 \cdot \delta}, \\ &= \frac{1}{N} \sum_{\tau, \sigma, \tau', \sigma'}^{i, \delta} V_\delta e^{-i(\mathbf{k}_3 - \mathbf{k}_4) \cdot \delta} \delta(\mathbf{k}_1 - \mathbf{k}_2 + \mathbf{k}_3 - \mathbf{k}_4) c_{\mathbf{k}_1, \tau, \sigma}^\dagger c_{\mathbf{k}_2, \tau, \sigma} c_{\mathbf{k}_3, \tau', \sigma'}^\dagger c_{\mathbf{k}_4, \tau', \sigma'}, \\ &= \frac{1}{N} \sum_{\delta, \mathbf{q}, \mathbf{k}, \mathbf{k}'} V_\delta e^{-i\mathbf{q} \cdot \delta} c_{\mathbf{k}, \tau, \sigma}^\dagger c_{\mathbf{k}+\mathbf{q}, \tau, \sigma} c_{\mathbf{k}', \tau', \sigma'}^\dagger c_{\mathbf{k}'-\mathbf{q}, \tau', \sigma'}, \\ &= \frac{1}{N} \sum_{\mathbf{q}} V(\mathbf{q}) \rho_{\mathbf{q}} \rho_{-\mathbf{q}}, \end{aligned} \quad (\text{C2})$$

where $V(\mathbf{q}) = \sum_{\delta} V_\delta e^{-i\mathbf{q} \cdot \delta}$, $\rho_{\pm\mathbf{q}} = \sum_{\mathbf{k}, \tau, \sigma} c_{\mathbf{k}, \tau, \sigma}^\dagger c_{\mathbf{k}\pm\mathbf{q}, \tau, \sigma}$, and \mathbf{q} and \mathbf{k} are defined in the whole momentum space.

The low-energy physics of TBG with alternative magnetic fluxes can also be effectively described by the Bistritzer-MacDonald (BM) model, which incorporates Dirac Hamiltonians with interlayer momentum couplings between the same valley Dirac points while neglecting the interlayer coupling between different valleys. In the basis of BM model, the interaction Hamiltonian Eq.C2 becomes

$$\hat{\mathcal{H}}_I = \frac{1}{2\Omega} \sum_{\mathbf{q}_M \in \text{MBZ}}^{\mathbf{g}} V(\mathbf{q}_M + \mathbf{g}) \delta \rho_{\mathbf{q}_M + \mathbf{g}} \delta \rho_{-\mathbf{q}_M - \mathbf{g}}, \quad \delta \rho_{\mathbf{q}_M + \mathbf{g}} = \sum_{\mathbf{k}_M \in \text{MBZ}}^{\eta, \tau, \mathbf{Q}} c_{\mathbf{k}_M + \mathbf{q}_M, \mathbf{Q} + \mathbf{g}, \tau, \eta}^\dagger c_{\mathbf{k}_M, \mathbf{Q}, \tau, \eta}, \quad (\text{C3})$$

where Ω denotes the total area of TBG. The symbol \mathbf{Q} indicates that the creation and annihilation operators originate from either the red or green Dirac cones, which are distinguished in the momentum lattice structure depicted in Fig. 1(d) of the main text. The momentums \mathbf{k}_M and \mathbf{q}_M are defined within the moiré BZ, while \mathbf{g} represents the moiré reciprocal vectors. Additionally, the index η corresponds to the valley index.

In the main text, we have presented a comprehensive analysis of the twisted bilayer graphene under alternative magnetic fluxes. Our investigation reveals the existence of eight-fold degenerate flat bands at zero energy per spin, each of which possesses a non-trivial Chern number owing to the presence of chiral symmetry. Additionally, the eight-fold degenerate flat bands introduce an effective orbital degree of freedom. Thus, we can characterize the eight-fold degenerate flat bands using the sublattice index ($\kappa = A$ and B), the effective orbital index ($\mu = o$ and o'), and the valley index ($\eta = K$ and K'). In the eight-fold degenerate flat

bands, the four bands that constitute Dirac points possess are marked by symbol o while the four bands originating from band inversion are marked by symbol o' . To distinguish from the unprojected interaction Hamiltonian $\hat{\mathcal{H}}_I$ with a hat, we represent the interaction Hamiltonian projected onto the eight-fold degenerate flat bands as \mathcal{H}_I without the hat. Then, the projected interaction Hamiltonian[4] is given by

$$\mathcal{H}_I = \frac{1}{2\Omega} \sum_{\mathbf{q}_M, \mathbf{g}} V(\mathbf{q}_M + \mathbf{g}) \delta \bar{\rho}_{\mathbf{q}_M + \mathbf{g}} \delta \bar{\rho}_{-\mathbf{q}_M - \mathbf{g}}, \quad \delta \bar{\rho}_{\mathbf{q}_M + \mathbf{g}} = \sum_{\mathbf{k}_M}^{\beta, \gamma} \{c_{\beta, \mathbf{k}_M}^\dagger [\Lambda_{\mathbf{q}_M + \mathbf{g}}(\mathbf{k}_M)]_{\beta, \gamma} c_{\gamma, \mathbf{k}_M + \mathbf{q}_M} - \nu \delta_{\mathbf{q}_M, 0} \delta_{\beta, \gamma}\}, \quad (\text{C4})$$

where $\beta = (\kappa, \mu, \eta)$ and $\gamma = (\kappa', \mu', \eta')$ contain the Chern number, orbital and valley indexes. $\delta \bar{\rho}_{\mathbf{q}_M + \mathbf{g}}$ denotes the Fourier components of the density operator projected into the eight-fold degenerate flat bands, while the background density at charge neutrality is denoted by ν . We can explicitly express $\delta \bar{\rho}_{\mathbf{q}_M + \mathbf{g}}$ by introducing the form factor $[\Lambda_{\mathbf{q}_M + \mathbf{g}}(\mathbf{k}_M)]_{\beta, \gamma} = \langle u_{\beta, \mathbf{k}_M} | u_{\gamma, \mathbf{k}_M + \mathbf{q}_M} \rangle$, where $|u_{\beta, \mathbf{k}_M}\rangle$ represents the periodic Bloch wave function associated with the flat band.

b. Ground states of intrasublattice-intraorbital interaction

We turn to derive the intrasublattice-intraorbital interaction Hamiltonian with chiral symmetry. We will examine how symmetries impose constraints on the structure of the form factor $\Lambda_{\mathbf{q}_M + \mathbf{g}}(\mathbf{k}_M)$, where we take chiral symmetry $S = \kappa_z \mu_0 \eta_0$, $C_2T = \kappa_x \mu_0 \eta_z K$ and $PT = \kappa_y \mu_0 \eta_x$ [5]. Under the influence of these symmetries, we obtain the following expression:

$$\begin{aligned} \langle u_{A, \mu, \eta, \mathbf{k}_M} | u_{B, \mu', \eta, \mathbf{k}_M + \mathbf{q}_M} \rangle &= \langle u_{A, \mu, \eta, \mathbf{k}_M} | S^2 | u_{B, \mu', \eta, \mathbf{k}_M + \mathbf{q}_M} \rangle = -\langle u_{A, \mu, \eta, \mathbf{k}_M} | u_{B, \mu', \eta, \mathbf{k}_M + \mathbf{q}_M} \rangle = 0, \\ \langle u_{\kappa, \mu, \eta, \mathbf{k}_M} | u_{\kappa', \mu', \eta, \mathbf{k}_M + \mathbf{q}_M} \rangle &= \langle u_{\kappa, \mu, \eta, \mathbf{k}_M} | (C_2T)^2 | u_{\kappa', \mu', \eta, \mathbf{k}_M + \mathbf{q}_M} \rangle = \langle u_{-\kappa, \mu, \eta, \mathbf{k}_M} | u_{-\kappa', \mu', \eta, \mathbf{k}_M + \mathbf{q}_M} \rangle^*, \\ \langle u_{\kappa, \mu, K, \mathbf{k}_M} | u_{\kappa, \mu, K, \mathbf{k}_M + \mathbf{q}_M} \rangle &= \langle u_{\kappa, \mu, K, \mathbf{k}_M} | (PT)^2 | u_{\kappa, \mu, K, \mathbf{k}_M + \mathbf{q}_M} \rangle = \langle u_{-\kappa, \mu, K', \mathbf{k}_M} | u_{-\kappa, \mu, K', \mathbf{k}_M + \mathbf{q}_M} \rangle, \\ \langle u_{\kappa, \mu, K, \mathbf{k}_M} | u_{-\kappa, \mu, K, \mathbf{k}_M + \mathbf{q}_M} \rangle &= \langle u_{\kappa, \mu, K, \mathbf{k}_M} | (PT)^2 | u_{-\kappa, \mu, K, \mathbf{k}_M + \mathbf{q}_M} \rangle = -\langle u_{-\kappa, \mu, K', \mathbf{k}_M} | u_{\kappa, \mu, K', \mathbf{k}_M + \mathbf{q}_M} \rangle. \end{aligned} \quad (\text{C5})$$

Based on the above constrain to the form factor $[\Lambda_{\pm \mathbf{q}_M \pm \mathbf{g}}(\mathbf{k}_M)]_{\beta, \gamma}$, the intrasublattice-intraorbital form factor in the same valley can be written as

$$\Lambda_{\pm \mathbf{q}_M \pm \mathbf{g}}^{\text{S, intra}}(\mathbf{k}_M) = \begin{pmatrix} \Delta & 0 & 0 & 0 & 0 & 0 & 0 & 0 \\ 0 & \Delta^* & 0 & 0 & 0 & 0 & 0 & 0 \\ 0 & 0 & \Delta & 0 & 0 & 0 & 0 & 0 \\ 0 & 0 & 0 & \Delta^* & 0 & 0 & 0 & 0 \\ 0 & 0 & 0 & 0 & \Delta^* & 0 & 0 & 0 \\ 0 & 0 & 0 & 0 & 0 & \Delta & 0 & 0 \\ 0 & 0 & 0 & 0 & 0 & 0 & \Delta^* & 0 \\ 0 & 0 & 0 & 0 & 0 & 0 & 0 & \Delta \end{pmatrix}, \quad \Delta = \langle u_{A, o, K, \mathbf{k}_M} | u_{A, o, K, \mathbf{k}_M \pm \mathbf{q}_M} \rangle = \langle u_{A, o', K, \mathbf{k}_M} | u_{A, o', K, \mathbf{k}_M \pm \mathbf{q}_M} \rangle \quad (\text{C6})$$

where the basis is $[c_{A, o, K}^\dagger, c_{B, o, K}^\dagger, c_{A, o', K}^\dagger, c_{B, o', K}^\dagger, c_{A, o, K'}^\dagger, c_{B, o, K'}^\dagger, c_{A, o', K'}^\dagger, c_{B, o', K'}^\dagger]$. By setting $\Delta = F_{\mathbf{q}_M}^{\text{intra}}(\mathbf{k}_M) e^{i\Phi_{\mathbf{q}_M}^{\text{intra}}(\mathbf{k}_M)}$, the form factor can be simplified to

$$\Lambda_{\mathbf{q}_M + \mathbf{g}}^{\text{S, intra}}(\mathbf{k}_M) = F_{\mathbf{q}_M}^{\text{intra}}(\mathbf{k}_M) e^{i\Phi_{\mathbf{q}_M}^{\text{intra}}(\mathbf{k}_M) \kappa_z \mu_0 \eta_z}, \quad (\text{C7})$$

Total Chern number		$C_T = \pm 2$	$C_T = \pm 1$	$C_T = 0$
Double FBs	Configuration number	2	\times	4
	Half filling of 4 bands each band with $C = \pm 1$	Two filled bands with $C = \pm 1$	\times	One filled band with $C = \pm 1$ another filled band with $C = \mp 1$
Quadruple FBs	Configuration number	$2 \times C_2^4 = 12$	$2 \times C_3^4 C_1^4 = 32$	$4 \times C_2^4 + 2 = 26$
	Half filling of 8 bands orbital o : $C = \pm 1$ orbital o' : $C = 0$	Two filled bands with $C = \pm 1$ two other filled bands with $C = 0$	Three filled bands with $C = \pm 1$ or ∓ 1 another filled bands with $C = 0$	One filled band with $C = \pm 1$ another filled band with $C = \mp 1$ two other filled bands with $C = 0$

TABLE S1: Comparison of ground states between double and quadruple flat bands at half-filling.

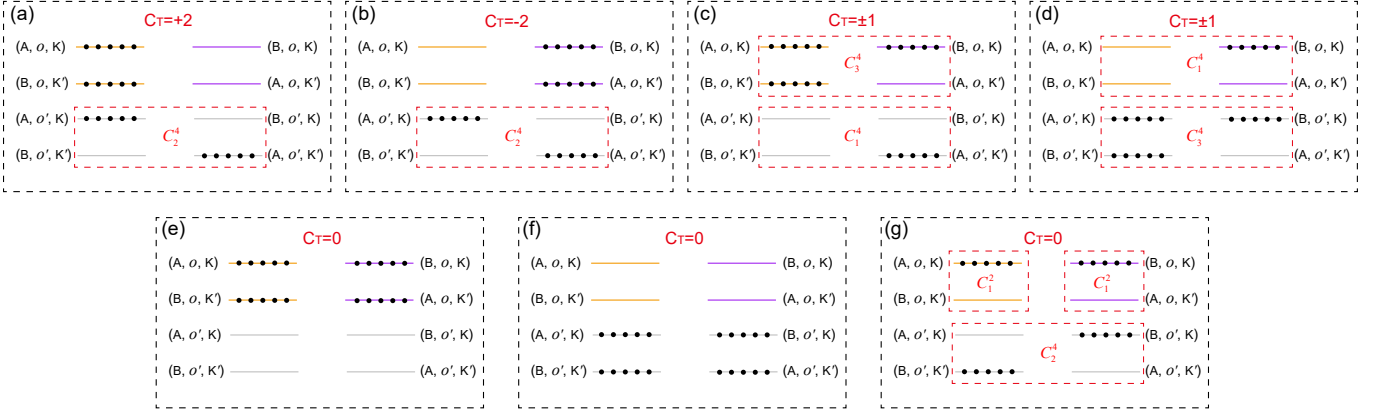


FIG. S10: (color online) The configurations for ground states with total Chern number $C_T = \pm 2$, $C_T = \pm 1$ and $C_T = 0$ in the quadratic flat bands at half-filling. The flat band labelled by gray, pink and orange lines possesses Chern number $C = 0$, $C = -1$, and $C = +1$, respectively.

and the intrasublattice-intraorbital interaction Hamiltonian can be written as

$$\mathcal{H}_I^{S,\text{intra}} = \frac{1}{2A} \sum_{\mathbf{q}_M, \mathbf{g}} V(\mathbf{q}_M + \mathbf{g}) \delta \bar{\rho}_{\mathbf{q}_M + \mathbf{g}}^{S,\text{intra}} \delta \bar{\rho}_{-\mathbf{q}_M - \mathbf{g}}^{S,\text{intra}}. \quad (\text{C8})$$

Then, we investigate ground states of Hamiltonian $\mathcal{H}_I^{S,\text{intra}}$ at charge-neutrality for the spinless case, where four out of eight flat bands are occupied. As this Hamiltonian can be expressed as a sum of positive semidefinite operators for each momentum \mathbf{q}_M , we can establish that any state satisfying $\delta \bar{\rho}_{\mathbf{q}_M + \mathbf{g}}^{S,\text{intra}} |\Psi\rangle = 0$ for all \mathbf{q}_M serves as a ground state. Subsequently, we explore possible ground states for filling four bands that satisfy $\delta \bar{\rho}_{\mathbf{q}_M + \mathbf{g}}^{S,\text{intra}} |\Psi\rangle = 0$ for all \mathbf{q}_M , along with their corresponding total Chern numbers.

Before explore all possible ground states, we discuss the comparison of ground states between double and quadruple flat bands at half-filling. According to established research[6], the conventional TBG has double degenerate flat bands in each of its two valleys. These bands possess a distinct Chern number (C) of ± 1 , due to the topological nature of the Dirac cone. On a half-filling scenario, taking into account both valleys, these four flat bands can be marked by sublattice index ($\kappa = A$ or B) and valley index ($\eta = K$ or K'). As detailed in Table S1, the fillings with a total Chern number $C_T = \pm 2$ correspond to two possible configurations, while those with $C_T = 0$ correspond to four possible configurations. Transitioning to our discussion of four-fold degeneracy, this elevated degree of degeneracy in the flat bands diversify the configurations for various ground states. Two of the flat bands for each valley exhibit a Chern number of ± 1 , linked to the topological nature of the Dirac cone. We have denoted these two non-trivial bands with the orbital o and the remaining two flat bands with $C = 0$ with orbital o' . Thus, considering both valleys, these eight bands can be represented with sublattice (A, B), valley (K, K'), and orbital (o, o') indices. Specifically, we focus on the half filling scenario for comparative study. Even outside this scenario, the quadruple flat bands lead to a variety of ground states. In the half filling, the filling configurations can be classified to three categories based on the total Chern numbers $C_T = \pm 2, \pm 1, 0$, as shown in Fig.S10.

1. For $C_T = \pm 2$: When two states fill orbital o with the same Chern number sign, the other states fill any two slots of the four in orbital o' with $C = 0$. This results in $2C_2^4 = 12$ possible ground states. These states are the quantum Hall (QH) states due to non-zero Chern number, and furtherly they can be labeled by type- n ($C_T = +2$), as well as type- n' states ($C_T = -2$), with the index n ranging from 1 to 6. Fig.S11(b)-(g) present the configurations for the type- n QH states. Concurrently, the configurations for type- n' states serve as complementary counterparts to the type- n states, achieved through a horizontal exchange of the occupied bands between the left and right bands. This category naturally breaks time-reversal symmetry T . In addition, type-(1 \sim 2)[Type-(1' \sim 2')] QH states can host two-fold rotational symmetry (C_{2z}), while other states will break this symmetry.
2. For $C_T = \pm 1$: This has two types of half filling. When one/three state(s) occupies any slot in orbital o and the remaining three/one fill(s) any slot in orbital o' , this yields $2C_3^4 C_1^4 = 32$ possible QH states. We also use the type- n and type- n' to label these QH states, with the index n ranging from 1 to 16, and Fig.S12 presents the configurations for all QH states. It is evident that this category breaks both time-reversal symmetry T and two-fold rotational symmetry (C_{2z}).
3. For $C_T = 0$: Three types of configurations arise. First, four filled states occupy all of orbital o . Second, four filled states fill in all of orbital o' . Third, when a state fills in one of the two slots in orbital o with $C = 1$ and another fills in one of the

two in orbital o with $C = -1$, the remaining states occupy two of the four slots in orbital o' . The total number of ground states is $1 + 1 + C_1^2 C_1^2 C_2^4 = 26$. These states can be labeled by type- n and type- n' , as shown in Fig.S13. For type-(1 ~ 6) states, under the horizontal exchange of the occupied bands between the left and right bands, these ground states are invariant, indicating that these states don't have complementary counterparts type-(1' ~ 6'). Furthermore, some of states can be classified as valley-polarized (VP) states, valley orbital (OP) states, valley-orbital locking (VOL) states, and valley Hall (VH) states, which correspond to type-(1 ~ 2), type-(3 ~ 4), type-(5 ~ 6), and type-(7 ~ 12)[type-(7' ~ 12')], respectively. Type-3 and Type-4 states exhibit time-reversal symmetry (T) and two-fold rotational symmetry (C_{2z}), while Type-(7 ~ 8)[Type-(7' ~ 8')] QH states only feature time-reversal symmetry (T), with all other states breaking both of these symmetries.

For ease of comparison, Table S1 tabulates the number of filling configurations. The quadruple flat bands present a richer tapestry of configurations, notably introducing systems with $C_T = \pm 1$, which is absent in the conventional TBG's double flat bands. Furthermore, Table.S2 presents energy corrections, total Chern numbers (C_T), and the operator $Q_n^{|C_T|}$ for the three categories of ground states, as will be discussed in the follow.

In addition, similar to the double flat bands[6], intervalley coherent (IVC) states can also be realized in the quadruple flat bands. Within the manifold of Chern zero states, composed of double flat bands, the T-IVC and K-IVC states can be described as XY aligned and anti-aligned orders. Since the flat bands labeled by o and o' orbitals are topological nontrivial and trivial, we can individually analyze IVC states in these two orbitals, including both time-reversal IVC (T-IVC) or Kramers IVC (K-IVC) states[6]. On one hand, when considering the QH state in the o orbital and the IVC state in the o' orbital, a mixture of the QH and IVC state is realized, in sharp contrast to the case of double flat bands. On the other band, a combination of various types of IVC states in these two orbitals can also be achieved. Table.S3 summarizes possible various IVC states with total Chern numbers and energy corrections at half filling, and Fig.S14 and Fig.S15 exhibit the filling configuration for each IVC state. In Fig.S14 and Fig.S15, we utilize IVC states as a basis to describe the flat bands[5, 6], facilitating the analysis of energy corrections, which are given by

$$\begin{aligned} c_{\pm,o,IVC}^\dagger &= \frac{1}{\sqrt{2}}[e^{-i\phi/2}c_{A,o,K}^\dagger \pm e^{i\phi/2}c_{B,o,K'}^\dagger], & c_{\pm,o,\overline{IVC}}^\dagger &= \frac{1}{\sqrt{2}}[e^{-i\phi/2}c_{B,o,K}^\dagger \pm e^{i\phi/2}c_{A,o,K'}^\dagger], \\ c_{\pm,o',IVC}^\dagger &= \frac{1}{\sqrt{2}}[e^{-i\phi/2}c_{A,o',K}^\dagger \pm e^{i\phi/2}c_{B,o',K'}^\dagger], & c_{\pm,o',\overline{IVC}}^\dagger &= \frac{1}{\sqrt{2}}[e^{-i\phi/2}c_{B,o',K}^\dagger \pm e^{i\phi/2}c_{A,o',K'}^\dagger]. \end{aligned} \quad (C9)$$

Total Chern number	Type of ground state	$Q_n^{ C_T }$	Energy correction	ξ_h	$\xi_{\Lambda^{S,\text{inter}}}$	ξ_{Λ^A}
$C_T = \pm 2$	Type-1 and -1'	$Q_1^2 = \kappa_z \mu_0 \eta_0$	$4\lambda_A - 4J$	-	+	-
	Type-2 and -2'	$Q_2^2 = \kappa_z \mu_z \eta_0$	$4\lambda_A + 4\lambda_S - 4J$	-	-	-
	Type-(3~4) and -(3' ~ 4')	$Q_{(3\sim 4)}^2$	$4\lambda_A + 2\lambda_S - 4J$	-	0	-
	Type-(5~6) and -(5' ~ 6')	$Q_{(5\sim 6)}^2$	$2\lambda_A + 2\lambda_S - 2J$	0	0	0
$C_T = \pm 1$	Type-(1~3) and -(1' ~ 3')	$Q_{(1\sim 3)}^1$	$2\lambda_A + 4\lambda_S - 2J$	0	-	0
	Type-(4~16) and -(4' ~ 16')	$Q_{(4\sim 16)}^1$	$2\lambda_A + 2\lambda_S - 2J$	0	0	0
$C_T = 0$	Type-(1~2) [VP]	$Q_{(1\sim 2)}^0$	0	+	+	+
	Type-(3~6) [OP/VOL]	$Q_{(3\sim 6)}^0$	$4\lambda_S$	+	-	+
	Type-7 and -7' [VH]	$Q_7^0 = \kappa_z \mu_0 \eta_z$	$4\lambda_A - 4J$	-	+	-
	Type-8 and -8' [VH]	$Q_8^0 = \kappa_z \mu_z \eta_z$	$4\lambda_A + 4\lambda_S - 4J$	-	-	-
	Type-(9~10) and -(9' ~ 10') [VH]	$Q_{(9\sim 10)}^0$	$4\lambda_A + 2\lambda_S - 4J$	-	0	-
	Type-(11~12) and -(11' ~ 12') [VH]	$Q_{(11\sim 12)}^0$	$2\lambda_A + 2\lambda_S - 2J$	0	0	0
	Type-(13~16) and -(13' ~ 16')	$Q_{(13\sim 16)}^0$	$2\lambda_A + 2\lambda_S - 2J$	0	0	0

TABLE S2: Energy corrections, total Chern numbers (C_T), and the operator $Q_n^{|C_T|}$ for the three categories of ground states. The symbols $\xi_x = +, -, 0$ indicate the different commutation relations between the operators $Q_n^{|C_T|}$ and x , namely commutation, anticommutation, and neither commutation nor anticommutation, where x denotes the single-particle dispersion h in Eq.C10, the form factor Λ^A in Eq.C20 and the form factor $\Lambda^{S,\text{inter}}$ in Eq.C29. The operator $Q_n^{|C_T|}$ depends on the configuration of corresponding ground states, and Table.S4 presents the corresponding operator $Q_n^{|C_T|}$ for each ground state.

Total Chern number	Intervalley-coherent state	Type-n	Energy correction
$C_T = \pm 2$	$[\text{QH}]_o[\text{T-IVC}]_{o'}$	Type-(1~4)	$4\lambda_A + 2\lambda_S - 2J$
	$[\text{QH}]_o[\text{K-IVC}]_{o'}$	Type-(1~4)	$2\lambda_A + 2\lambda_S - 4J$
$C_T = 0$	$[\text{T-IVC}]_o[\text{T-IVC}]_{o'}$	Type-(1~2)	$4\lambda_A + 4\lambda_S$
		Type-(3~4)	$4\lambda_A$
	$[\text{T-IVC}]_o[\text{K-IVC}]_{o'}$	Type-(1~2)	$2\lambda_A + 2\lambda_S - 2J$
	$[\text{K-IVC}]_o[\text{T-IVC}]_{o'}$	Type-(1~4)	$2\lambda_A + 2\lambda_S - 2J$
	$[\text{K-IVC}]_o[\text{K-IVC}]_{o'}$	Type-(1~2)	$4\lambda_S - 4J$
		Type-(3~4)	$-4J$

TABLE S3: Total Chern numbers (C_T) and energy corrections in various IVC states.

where the phase ϕ is related to the angle of the IVC order in the x - y plane. Subsequently, these IVC states can be categorized into two groups based on the total Chern numbers $C_T = \pm 2, 0$, and each category encompasses distinct types of filling configurations, as illustrated in Table.S3. For IVC states with $C_T = \pm 2$, we consider the QH state with $C_T = \pm 2$ in the o orbital, and T-IVC or K-IVC states in the o' orbital, denoted as $[\text{QH}]_o[\text{T-IVC}]_{o'}$ and $[\text{QH}]_o[\text{K-IVC}]_{o'}$. Furthermore, each IVC state can accommodate four types of filling configurations, as illustrated in Fig.S14. As for IVC states with $C_T = 0$, we consider T-IVC or K-IVC states in the o and o' orbital, resulting in four distinct IVC states denoted as $[\text{T-IVC}]_o[\text{T-IVC}]_{o'}$, $[\text{T-IVC}]_o[\text{K-IVC}]_{o'}$, $[\text{K-IVC}]_o[\text{T-IVC}]_{o'}$ and $[\text{K-IVC}]_o[\text{K-IVC}]_{o'}$. Moreover, each IVC state can also host four types of filling configurations, as presented in Fig.S15.

2. Energy correction of ground states

Here, we investigate the energy correction of ground states induced by three perturbations, including single-particle dispersion, intersublattice-intraorbital and intrasublattice-interorbital interactions. We make a key assumption that the magnitude of these terms is significantly smaller compared to the interaction scale, allowing them to be treated as perturbations. Furthermore, we present an intuitive picture to understand the energy correction.

a. Single-particle dispersion

In the basis $\psi_{\mathbf{k}_M}^\dagger = [c_{A,o,K,\mathbf{k}_M}^\dagger, c_{B,o,K,\mathbf{k}_M}^\dagger, c_{A,o',K,\mathbf{k}_M}^\dagger, c_{B,o',K,\mathbf{k}_M}^\dagger, c_{A,o,K',\mathbf{k}_M}^\dagger, c_{B,o,K',\mathbf{k}_M}^\dagger, c_{A,o',K',\mathbf{k}_M}^\dagger, c_{B,o',K',\mathbf{k}_M}^\dagger]$, then the single-particle dispersion can be written as $\mathcal{H}_0 = \sum_{\mathbf{k}_M} \psi_{\mathbf{k}_M}^\dagger h(\mathbf{k}_M) \psi_{\mathbf{k}_M}$. Under the constrain of chiral symmetry and PT symmetry, the matrix $h(\mathbf{k}_M)$ can be given by

$$h(\mathbf{k}_M) = \begin{pmatrix} 0 & t(\mathbf{k}_M) & 0 & 0 & 0 & 0 & 0 & 0 \\ t^*(\mathbf{k}_M) & 0 & 0 & 0 & 0 & 0 & 0 & 0 \\ 0 & 0 & 0 & t(\mathbf{k}_M) & 0 & 0 & 0 & 0 \\ 0 & 0 & t^*(\mathbf{k}_M) & 0 & 0 & 0 & 0 & 0 \\ 0 & 0 & 0 & 0 & 0 & t^*(\mathbf{k}_M) & 0 & 0 \\ 0 & 0 & 0 & 0 & t(\mathbf{k}_M) & 0 & 0 & 0 \\ 0 & 0 & 0 & 0 & 0 & 0 & 0 & t^*(\mathbf{k}_M) \\ 0 & 0 & 0 & 0 & 0 & 0 & t(\mathbf{k}_M) & 0 \end{pmatrix} = h_x(\mathbf{k}_M)\kappa_x\mu_0\eta_0 + h_y(\mathbf{k}_M)\kappa_y\mu_0\eta_0\mathcal{C}10$$

where $t(\mathbf{k}_M) = h_x(\mathbf{k}_M) - ih_y(\mathbf{k}_M)$ with real functions $h_x(\mathbf{k}_M)$ and $h_y(\mathbf{k}_M)$, and we only consider the intra-orbital hopping $t(\mathbf{k}_M)$ in the same valley.

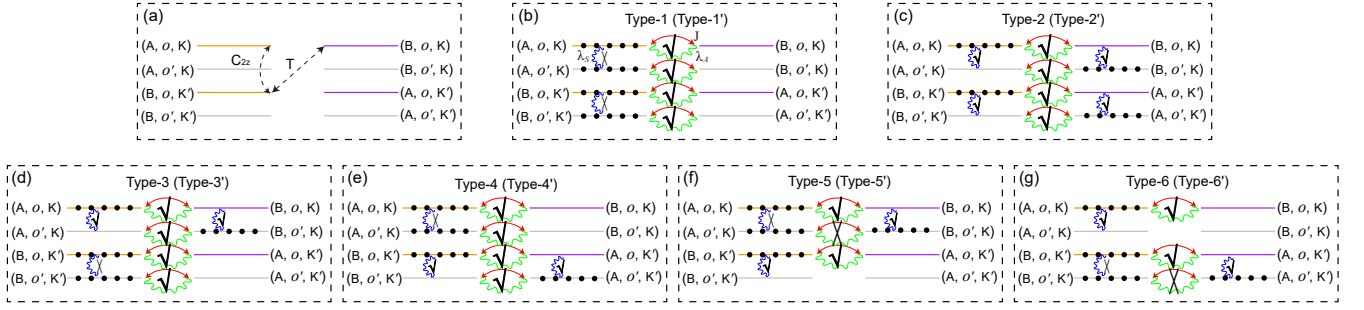


FIG. S11: (color online) (a) In the spinless flat band basis labelled by sublattice (A, B), valley (K, K'), and orbital (o, o') indices, the behavior of time-reversal symmetry (T) and two-fold rotational symmetry (C_{2z}) is illustrated. (b)-(g) The 12 QH states, characterized by total Chern number $C_T = \pm 2$, are categorized as type- n ($C_T = +2$) and type- n' ($C_T = -2$), with n ranging from 1 to 6. The type- n' states correspond as complementary counterparts to the type- n states, and they can be generated by horizontally exchanging the occupied bands between the left and right bands. The flat band labelled by gray, orange and pink lines possesses Chern number $C = 0, C = +1$, and $C = -1$. The red curves represent the single-particle dispersion, while the green and blue wavy lines correspond to the intersublattice-intraorbital and intrasublattice-interorbital interactions. The parameters of J, λ_A and λ_S are the strength of the corresponding perturbation within the basis. The symbols \sqrt or \times indicate whether the processes are permitted or forbidden.

The analysis of the aforementioned ground states primarily focuses on the intrasublattice-intraorbital interaction, neglecting the effects of single-particle dispersion. To account for the influence of single-particle dispersion, we employ second-order perturbation theory to evaluate the perturbative correction to the energy. Then, this correction can be expressed as

$$\Delta E = \sum'_n \frac{\langle \psi^{(0)} | \mathcal{H}_0 | \psi_n^{(0)} \rangle \langle \psi_n^{(0)} | \mathcal{H}_0 | \psi^{(0)} \rangle}{E^{(0)} - E_n^{(0)}}. \quad (\text{C11})$$

Here, the symbol $\psi^{(0)}$ represents the unperturbed ground state, \mathcal{H}_0 denotes the perturbation Hamiltonian, $\psi_n^{(0)}$ represents the unperturbed excited states, and $E^{(0)}$ and $E_n^{(0)}$ correspond to the unperturbed ground state energy and excited state energies, respectively. Let us delve into the analysis of the Eq.C11.

Firstly, the single-particle Hamiltonian \mathcal{H}_0 establishes connections between bands with different sublattice within the same orbital and valley, which can be simplified to

$$\mathcal{H}_0 = \sum_{\mathbf{k}_M} \{ [h_x(\mathbf{k}_M) - ih_y(\mathbf{k}_M)] c_{A,\mathbf{k}_M}^\dagger c_{B,\mathbf{k}_M} + h.c. \}. \quad (\text{C12})$$

For convenience, we have omitted the symbols μ and η .

Secondly, considering the simplified basis operator $\psi_{\mathbf{k}_M}^\dagger = [c_{A,\mathbf{k}_M}^\dagger, c_{B,\mathbf{k}_M}^\dagger]$, there are three ground states, namely $|\Psi_A\rangle = \prod_{\mathbf{k}_M} c_{\mathbf{k}_M,A}^\dagger |0\rangle$, $|\Psi_B\rangle = \prod_{\mathbf{k}_M} c_{\mathbf{k}_M,B}^\dagger |0\rangle$ and $|\Psi_{A/B}\rangle = \prod_{\mathbf{k}_M} c_{\mathbf{k}_M,A}^\dagger c_{\mathbf{k}_M,B}^\dagger |0\rangle$. If a state exhibits both bands connected by \mathcal{H}_0 being either completely filled or completely empty, it will be annihilated by the perturbation operator \mathcal{H}_0 due to the complete blocked of tunneling processes. Consequently, only the states $|\Psi_A\rangle$ and $|\Psi_B\rangle$ can contribute to the energy correction induced by the perturbation \mathcal{H}_0 . For the purpose of illustration, we consider $|\psi^{(0)}\rangle = |\Psi_A\rangle$ as an exemplary case.

Thirdly, by applying the perturbation \mathcal{H}_0 to the state $|\psi^{(0)}\rangle = |\Psi_A\rangle$, we can obtain

$$H_0 |\Psi_A\rangle = \sum_{\mathbf{k}_M} [h_x(\mathbf{k}_M) + ih_y(\mathbf{k}_M)] \Psi_{\mathbf{k}_M,\text{eh}}, \quad |\Psi_{\mathbf{k}_M,\text{eh}}\rangle = c_{\mathbf{k}_M,B}^\dagger c_{\mathbf{k}_M,A} |\Psi_A\rangle, \quad (\text{C13})$$

where $|\Psi_{\mathbf{k}_M,\text{eh}}\rangle$ represents an unperturbed excited state containing an electron-hole pair with momentum \mathbf{k}_M . Consequently, we can utilize $|\psi_n^{(0)}\rangle = |\Psi_{\mathbf{k}_M,\text{eh}}\rangle$ to calculate the energy correction described by Eq.C11. Moreover, it is worth noting that $E^{(0)}$ in Eq.C11 should be zero, as we consider the zero-energy flat bands.

Finally, based on the preceding discussion, we can derive the expression for the energy correction resulting from single-particle dispersion in the flat bands, which is given by

$$\Delta E = -J = -\frac{1}{N} \sum_{\mathbf{k}_M, \mathbf{k}'_M} \frac{[h_x(\mathbf{k}_M) + ih_y(\mathbf{k}_M)][h_x(\mathbf{k}'_M) - ih_y(\mathbf{k}'_M)]}{\langle \Psi_{\mathbf{k}_M,\text{eh}} | \mathcal{H}_I^{\text{S,intra}} | \Psi_{\mathbf{k}'_M,\text{eh}} \rangle}. \quad (\text{C14})$$

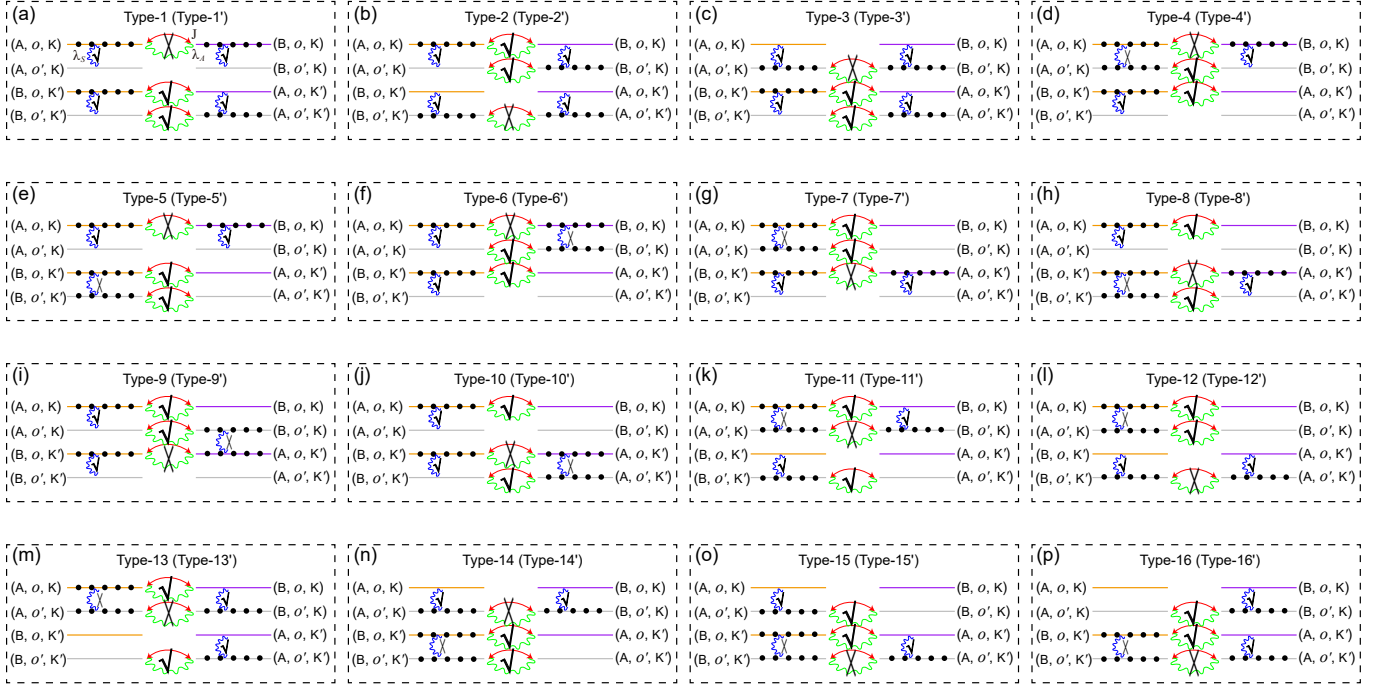


FIG. S12: (color online) (a)-(p) The 32 QH states, characterized by total Chern number $C_T = \pm 1$, are categorized as type- n ($C_T = +1$) and type- n' ($C_T = -1$), with n ranging from 1 to 16. The type- n' states correspond as complementary counterparts to the type- n states, and they can be generated by horizontally shifting the occupied bands between the left and right bands.

Hence, by using Eq.C14, we can obtain the energy correction of all ground states induced by single-particle dispersion, as shown in Table.S2.

Similarly, for various IVC states, we can also obtain the energy correction induced by single-particle dispersion, as shown in Table.S3.

b. Intersublattice-intraorbital interaction

To account for the influence of intersublattice-intraorbital interaction, we employ first-order perturbation theory to evaluate the perturbative correction to the energy. Then, this correction can be expressed as

$$\Delta E^A = \langle \psi^{(0)} | \mathcal{H}_I^A | \psi^{(0)} \rangle, \quad (\text{C15})$$

where the symbol $\psi^{(0)}$ represents the unperturbed ground state, \mathcal{H}_I^A denotes the intersublattice-intraorbital interaction Hamiltonian. Based on the symmetry relationships Eq.C5, the intersublattice-intraorbital projected interaction Hamiltonian without chiral symmetry in the same valley and orbital can be written as

$$\mathcal{H}_I^A = \frac{1}{2\Omega} \sum_{\mathbf{q}_M, \mathbf{g}} V(\mathbf{q}_M + \mathbf{g}) \delta \bar{\rho}_{\mathbf{q}_M + \mathbf{g}}^A \delta \bar{\rho}_{-\mathbf{q}_M - \mathbf{g}}^A, \quad \delta \bar{\rho}_{\pm \mathbf{q}_M \pm \mathbf{g}}^A = \sum_{\mathbf{k}_M} c_{\beta, \mathbf{k}_M}^\dagger [\Lambda_{\pm \mathbf{q}_M \pm \mathbf{g}}^A(\mathbf{k}_M)]_{\beta, \gamma} c_{\gamma, \mathbf{k}_M \pm \mathbf{q}_M} \quad (\text{C16})$$

$$\Lambda_{\pm \mathbf{q}_M \pm \mathbf{g}}^A(\mathbf{k}_M) = \begin{pmatrix} 0 & \Delta_{\pm} & 0 & 0 & 0 & 0 & 0 & 0 \\ \Delta_{\pm}^* & 0 & 0 & 0 & 0 & 0 & 0 & 0 \\ 0 & 0 & 0 & \Delta_{\pm} & 0 & 0 & 0 & 0 \\ 0 & 0 & \Delta_{\pm}^* & 0 & 0 & 0 & 0 & 0 \\ 0 & 0 & 0 & 0 & 0 & -\Delta_{\pm}^* & 0 & 0 \\ 0 & 0 & 0 & 0 & -\Delta_{\pm} & 0 & 0 & 0 \\ 0 & 0 & 0 & 0 & 0 & 0 & 0 & -\Delta_{\pm}^* \\ 0 & 0 & 0 & 0 & 0 & 0 & -\Delta_{\pm} & 0 \end{pmatrix}, \quad \Delta_{\pm} = \langle u_{A, o/o', K, \mathbf{k}_M} | u_{B, o/o', K, \mathbf{k}_M \pm \mathbf{q}_M} \rangle, \quad (\text{C17})$$

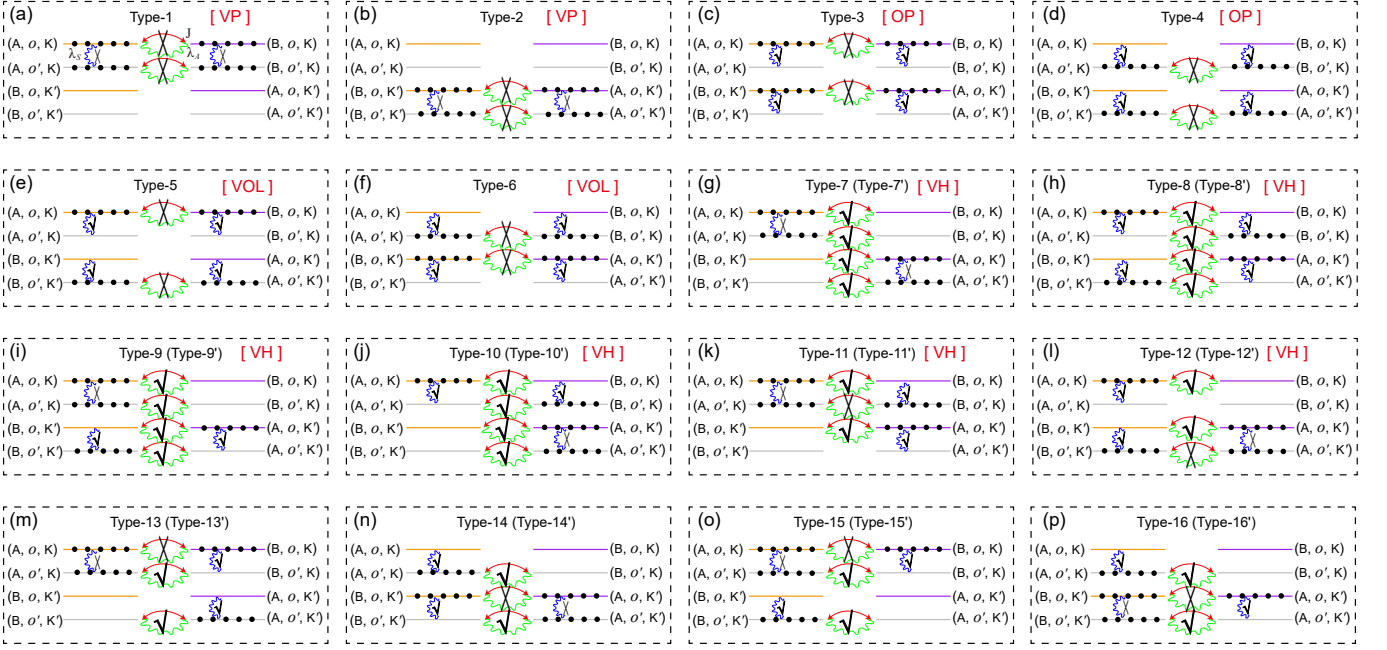


FIG. S13: (color online) (a)-(p) 26 ground states with zero total Chern number. The type- n' ($n = 7 \sim 16$) states correspond as complementary counterparts to the type- n states, and they can be generated by horizontally shifting the occupied bands between the left and right bands.

where the band basis is $\psi_{\mathbf{k}_M}^\dagger = [c_{A,o,K,\mathbf{k}_M}^\dagger, c_{B,o,K,\mathbf{k}_M}^\dagger, c_{A,o',K,\mathbf{k}_M}^\dagger, c_{B,o',K,\mathbf{k}_M}^\dagger, c_{A,o,K',\mathbf{k}_M}^\dagger, c_{B,o,K',\mathbf{k}_M}^\dagger, c_{A,o',K',\mathbf{k}_M}^\dagger, c_{B,o',K',\mathbf{k}_M}^\dagger]$. By setting $\Delta_{\pm} = F_{\pm\mathbf{q}_M}^A(\mathbf{k}_M)e^{-i\Phi_{\mathbf{q}_M}^A(\pm\mathbf{k}_M)}$, and then $\langle u_{A,o/o',K,\mathbf{k}_M-\mathbf{q}_M} | u_{B,o/o',K,\mathbf{k}_M} \rangle = F_{\mathbf{q}_M}^A(\mathbf{k}_M - \mathbf{q}_M)e^{-i\Phi_{\mathbf{q}_M}^A(\mathbf{k}_M - \mathbf{q}_M)}$, which can be further written as

$$\langle u_{A,o/o',K,\mathbf{k}_M-\mathbf{q}_M} | u_{B,o/o',K,\mathbf{k}_M} \rangle = \langle u_{B,o/o',K,\mathbf{k}_M} | u_{A,o/o',K,\mathbf{k}_M-\mathbf{q}_M} \rangle^* = \Delta_- = F_{-\mathbf{q}_M}^A(\mathbf{k}_M)e^{-i\Phi_{\mathbf{q}_M}^A(-\mathbf{k}_M)}. \quad (\text{C18})$$

Hence, we can get

$$F_{\mathbf{q}_M}^A(\mathbf{k}_M - \mathbf{q}_M) = F_{-\mathbf{q}_M}^A(\mathbf{k}_M), \quad e^{-i\Phi_{\mathbf{q}_M}^A(\mathbf{k}_M - \mathbf{q}_M)} = e^{-i\Phi_{-\mathbf{q}_M}^A(\mathbf{k}_M)}. \quad (\text{C19})$$

Then, the intra-orbital form factor can be simplified to

$$\Lambda_{\pm\mathbf{q}_M \pm \mathbf{g}}^A(\mathbf{k}_M) = \kappa_x \mu_0 \eta_z F_{\pm\mathbf{q}_M}^A(\mathbf{k}_M) e^{i\Phi_{\pm\mathbf{q}_M}^A(\mathbf{k}_M) \kappa_x \mu_0 \eta_z}. \quad (\text{C20})$$

Then,

$$\begin{aligned} \delta \bar{\rho}_{\mathbf{q}_M + \mathbf{g}}^{-A} &= \sum_{\mathbf{k}_M}^{\mu} F_{\mathbf{q}_M}^A(\mathbf{k}_M) [e^{-i\Phi_{\mathbf{q}_M}^A(\mathbf{k}_M)} (c_{A,\mu,K,\mathbf{k}_M}^\dagger c_{B,\mu,K,\mathbf{k}_M+\mathbf{q}_M} - c_{B,\mu,K',\mathbf{k}_M}^\dagger c_{A,\mu,K',\mathbf{k}_M+\mathbf{q}_M}) \\ &\quad + e^{i\Phi_{\mathbf{q}_M}^A(\mathbf{k}_M)} (c_{B,\mu,K,\mathbf{k}_M}^\dagger c_{A,\mu,K,\mathbf{k}_M+\mathbf{q}_M} - c_{A,\mu,K',\mathbf{k}_M}^\dagger c_{B,\mu,K',\mathbf{k}_M+\mathbf{q}_M})], \\ \delta \bar{\rho}_{-\mathbf{q}_M - \mathbf{g}}^{-A} &= \sum_{\mathbf{k}_M}^{\mu} F_{-\mathbf{q}_M}^A(\mathbf{k}_M) [e^{-i\Phi_{-\mathbf{q}_M}^A(\mathbf{k}_M)} (c_{A,\mu,K,\mathbf{k}_M}^\dagger c_{B,\mu,K,\mathbf{k}_M-\mathbf{q}_M} - c_{B,\mu,K',\mathbf{k}_M}^\dagger c_{A,\mu,K',\mathbf{k}_M-\mathbf{q}_M}) \\ &\quad + e^{i\Phi_{-\mathbf{q}_M}^A(\mathbf{k}_M)} (c_{B,\mu,K,\mathbf{k}_M}^\dagger c_{A,\mu,K,\mathbf{k}_M-\mathbf{q}_M} - c_{A,\mu,K',\mathbf{k}_M}^\dagger c_{B,\mu,K',\mathbf{k}_M-\mathbf{q}_M})] \end{aligned} \quad (\text{C21})$$

Here, we turn to calculate ΔE^A equation Eq.C15. We take type-1 QH state with total Chern number $C_T = 1$ as example, and the wave function can be written as $|\Psi_{\text{type-1}}^{C=1}\rangle = \prod_{\mathbf{k}_M} c_{A,o,K,\mathbf{k}_M}^\dagger c_{A,o',K',\mathbf{k}_M}^\dagger c_{B,o,K',\mathbf{k}_M}^\dagger c_{B,o,K,\mathbf{k}_M}^\dagger |0\rangle$. Then, the derivation process

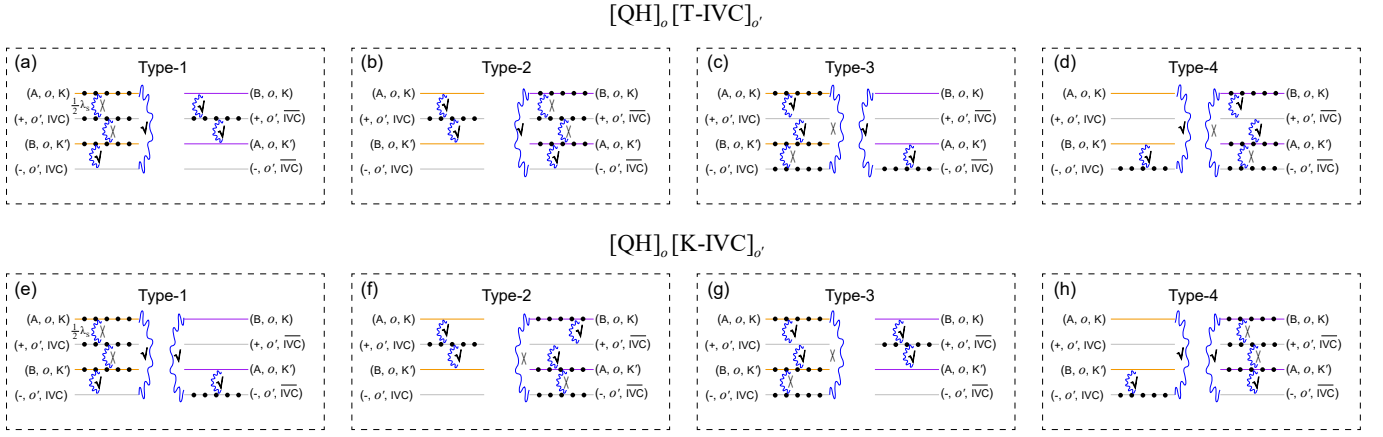


FIG. S14: (color online) The filling configurations for IVC states with $C_T = \pm 2$, and we use IVC states as basis to describe o' -orbital flat bands. The blue wavy line corresponds to the intrasublattice-interorbital interactions, and the symbols \surd or \times indicate whether the processes are permitted or forbidden.

is as follows

$$\begin{aligned}
& \delta \bar{\rho}_{\mathbf{q}_M + \mathbf{g}}^A |\Psi_{\text{type-1}}^{C=1}\rangle, \\
& = \sum_{\mathbf{k}_M} F_{\mathbf{q}_M}^A(\mathbf{k}_M) [-e^{-i\Phi_{\mathbf{q}_M}^A(\mathbf{k}_M)} c_{B,o',K',\mathbf{k}_M}^\dagger c_{A,o',K',\mathbf{k}_M + \mathbf{q}_M} - e^{i\Phi_{\mathbf{q}_M}^A(\mathbf{k}_M)} c_{A,o,K',\mathbf{k}_M}^\dagger c_{B,o,K',\mathbf{k}_M + \mathbf{q}_M}] |\Psi_{\text{type-1}}^{C=1}\rangle, \\
& \delta \bar{\rho}_{-\mathbf{q}_M - \mathbf{g}}^A |\Psi_{\text{type-1}}^{C=1}\rangle, \\
& = \sum_{\mathbf{k}_M} F_{-\mathbf{q}_M}^A(\mathbf{k}_M) [-e^{-i\Phi_{-\mathbf{q}_M}^A(\mathbf{k}_M)} c_{B,o',K',\mathbf{k}_M}^\dagger c_{A,o',K',\mathbf{k}_M - \mathbf{q}_M} - e^{i\Phi_{-\mathbf{q}_M}^A(\mathbf{k}_M)} c_{A,o,K',\mathbf{k}_M}^\dagger c_{B,o,K',\mathbf{k}_M - \mathbf{q}_M}] |\Psi_{\text{type-1}}^{C=1}\rangle \quad (\text{C22})
\end{aligned}$$

where we can omit other terms due to the properties of fermions ($c^\dagger c^\dagger |0\rangle = 0$ and $c|0\rangle = 0$). Therefore, we obtain

$$\begin{aligned}
& \langle \Psi_{\text{type-1}}^{C=1} | \delta \bar{\rho}_{\mathbf{q}_M + \mathbf{g}}^A \delta \bar{\rho}_{-\mathbf{q}_M - \mathbf{g}}^A | \Psi_{\text{type-1}}^{C=1} \rangle, \\
& = \langle \Psi_{\text{type-1}}^{C=1} | \left\{ \sum_{\mathbf{k}'_M} F_{\mathbf{q}_M}^A(\mathbf{k}'_M) [-e^{i\Phi_{\mathbf{q}_M}^A(\mathbf{k}'_M)} c_{A,o',K',\mathbf{k}'_M}^\dagger c_{B,o',K',\mathbf{k}'_M + \mathbf{q}_M} - e^{-i\Phi_{\mathbf{q}_M}^A(\mathbf{k}'_M)} c_{B,o,K',\mathbf{k}'_M}^\dagger c_{A,o,K',\mathbf{k}'_M + \mathbf{q}_M}] \right\} \\
& \left\{ \sum_{\mathbf{k}_M} F_{-\mathbf{q}_M}^A(\mathbf{k}_M) [-e^{-i\Phi_{-\mathbf{q}_M}^A(\mathbf{k}_M)} c_{B,o',K',\mathbf{k}_M}^\dagger c_{A,o',K',\mathbf{k}_M - \mathbf{q}_M} - e^{i\Phi_{-\mathbf{q}_M}^A(\mathbf{k}_M)} c_{A,o,K',\mathbf{k}_M}^\dagger c_{B,o,K',\mathbf{k}_M - \mathbf{q}_M}] \right\} | \Psi_{\text{type-1}}^{C=1} \rangle, \\
& = \langle \Psi_{\text{type-1}}^{C=1} | \left\{ \sum_{\mathbf{k}'_M} F_{\mathbf{q}_M}^A(\mathbf{k}'_M) [e^{i\Phi_{\mathbf{q}_M}^A(\mathbf{k}'_M)} c_{A,o',K',\mathbf{k}'_M}^\dagger c_{B,o',K',\mathbf{k}'_M + \mathbf{q}_M}] \right\} \left\{ \sum_{\mathbf{k}_M} F_{-\mathbf{q}_M}^A(\mathbf{k}_M) [e^{-i\Phi_{-\mathbf{q}_M}^A(\mathbf{k}_M)} c_{B,o',K',\mathbf{k}_M}^\dagger c_{A,o',K',\mathbf{k}_M - \mathbf{q}_M}] \right\} \\
& + \left\{ \sum_{\mathbf{k}'_M} F_{\mathbf{q}_M}^A(\mathbf{k}'_M) e^{-i\Phi_{\mathbf{q}_M}^A(\mathbf{k}'_M)} c_{B,o,K',\mathbf{k}'_M}^\dagger c_{A,o,K',\mathbf{k}'_M + \mathbf{q}_M} \right\} \left\{ \sum_{\mathbf{k}_M} F_{-\mathbf{q}_M}^A(\mathbf{k}_M) [e^{i\Phi_{-\mathbf{q}_M}^A(\mathbf{k}_M)} c_{A,o,K',\mathbf{k}_M}^\dagger c_{B,o,K',\mathbf{k}_M - \mathbf{q}_M}] \right\} | \Psi_{\text{type-1}}^{C=1} \rangle, \\
& = \sum_{\mathbf{k}_M} \langle \Psi_{\text{type-1}}^{C=1} | \left\{ F_{\mathbf{q}_M}^A(\mathbf{k}_M - \mathbf{q}_M) [e^{i\Phi_{\mathbf{q}_M}^A(\mathbf{k}_M - \mathbf{q}_M)} c_{A,o',K',\mathbf{k}_M - \mathbf{q}_M}^\dagger c_{B,o',K',\mathbf{k}_M}^\dagger] \right\} \left\{ F_{-\mathbf{q}_M}^A(\mathbf{k}_M) [e^{-i\Phi_{-\mathbf{q}_M}^A(\mathbf{k}_M)} c_{B,o',K',\mathbf{k}_M}^\dagger c_{A,o',K',\mathbf{k}_M - \mathbf{q}_M}] \right\} \\
& + \left\{ F_{\mathbf{q}_M}^A(\mathbf{k}_M - \mathbf{q}_M) e^{-i\Phi_{\mathbf{q}_M}^A(\mathbf{k}_M - \mathbf{q}_M)} c_{B,o,K',\mathbf{k}_M - \mathbf{q}_M}^\dagger c_{A,o,K',\mathbf{k}_M}^\dagger \right\} \left\{ F_{-\mathbf{q}_M}^A(\mathbf{k}_M) [e^{i\Phi_{-\mathbf{q}_M}^A(\mathbf{k}_M)} c_{A,o,K',\mathbf{k}_M}^\dagger c_{B,o,K',\mathbf{k}_M - \mathbf{q}_M}] \right\} | \Psi_{\text{type-1}}^{C=1} \rangle, \\
& = \sum_{\mathbf{k}_M} [F_{-\mathbf{q}_M}^A(\mathbf{k}_M)]^2 \langle \Psi_{\text{type-1}}^{C=1} | n_{A,o',K',\mathbf{k}_M - \mathbf{q}_M} (1 - n_{B,o',K',\mathbf{k}_M}) + n_{B,o',K',\mathbf{k}_M - \mathbf{q}_M} (1 - n_{A,o',K',\mathbf{k}_M}) | \Psi_{\text{type-1}}^{C=1} \rangle. \quad (\text{C23})
\end{aligned}$$

In the second step, we have excluded terms that are inherently zero. Subsequently, in the third step, we substitute \mathbf{k}'_M with $\mathbf{k}_M - \mathbf{q}_M$. Finally, in the fourth step, we make use of the relationships as defined in Eq. C19.

$$\Lambda_{\pm\mathbf{q}_M\pm\mathbf{g}}^{\text{S,inter}}(\mathbf{k}_M) = \begin{pmatrix} 0 & \Delta_{\pm,1} & 0 & 0 & 0 & 0 & 0 & 0 \\ \Delta_{\pm,2} & 0 & 0 & 0 & 0 & 0 & 0 & 0 \\ 0 & 0 & 0 & \Delta_{\pm,1}^* & 0 & 0 & 0 & 0 \\ 0 & 0 & \Delta_{\pm,2}^* & 0 & 0 & 0 & 0 & 0 \\ 0 & 0 & 0 & 0 & 0 & -\Delta_{\pm,1}^* & 0 & 0 \\ 0 & 0 & 0 & 0 & -\Delta_{\pm,2}^* & 0 & 0 & 0 \\ 0 & 0 & 0 & 0 & 0 & 0 & 0 & -\Delta_{\pm,1} \\ 0 & 0 & 0 & 0 & 0 & 0 & -\Delta_{\pm,2} & 0 \end{pmatrix}, \quad (\text{C26})$$

where $\Delta_{\pm,1} = \langle u_{A,o,K,\mathbf{k}_M} | u_{A,o',K,\mathbf{k}_M\pm\mathbf{q}_M} \rangle$, $\Delta_{\pm,2} = \langle u_{A,o',K,\mathbf{k}_M} | u_{A,o,K,\mathbf{k}_M\pm\mathbf{q}_M} \rangle$, and the band basis is $\psi_{\mathbf{k}_M}^\dagger = [c_{A,o,K}^\dagger, c_{A,o',K}^\dagger, c_{B,o,K}^\dagger, c_{B,o',K}^\dagger, c_{A,o,K'}^\dagger, c_{A,o',K'}^\dagger, c_{B,o,K'}^\dagger, c_{B,o',K'}^\dagger]$. By setting $\Delta_{\pm,1} = \Delta_{\pm,2}^* = F_{\pm\mathbf{q}_M}^{\text{S}}(\mathbf{k}_M)e^{i\Phi_{\pm\mathbf{q}_M}^{\text{S}}(\mathbf{k}_M)}$, which can be further written as

$$\begin{aligned} F_{\mathbf{q}_M}^{\text{S}}(\mathbf{k}_M - \mathbf{q}_M)e^{i\Phi_{\mathbf{q}_M}^{\text{S}}(\mathbf{k}_M - \mathbf{q}_M)} &= \langle u_{A,o,K,\mathbf{k}_M - \mathbf{q}_M} | u_{A,o',K,\mathbf{k}_M} \rangle, \\ &= \langle u_{A,o',K,\mathbf{k}_M} | u_{A,o,K,\mathbf{k}_M - \mathbf{q}_M} \rangle^* = F_{-\mathbf{q}_M}^{\text{S}}(\mathbf{k}_M)e^{i\Phi_{-\mathbf{q}_M}^{\text{S}}(\mathbf{k}_M)}. \end{aligned} \quad (\text{C27})$$

Hence, we can get

$$F_{\mathbf{q}_M}^{\text{S}}(\mathbf{k}_M - \mathbf{q}_M) = F_{-\mathbf{q}_M}^{\text{S}}(\mathbf{k}_M), \quad e^{i\Phi_{\mathbf{q}_M}^{\text{S}}(\mathbf{k}_M - \mathbf{q}_M)} = e^{i\Phi_{-\mathbf{q}_M}^{\text{S}}(\mathbf{k}_M)}. \quad (\text{C28})$$

Then, the inter-orbital form factor can be simplified to

$$\Lambda_{\pm\mathbf{q}_M\pm\mathbf{g}}^{\text{S,inter}}(\mathbf{k}_M) = \mu_x \kappa_0 \eta_z F_{\pm\mathbf{q}_M}^{\text{S}}(\mathbf{k}_M) e^{i\Phi_{\pm\mathbf{q}_M}^{\text{S}}(\mathbf{k}_M) \mu_z \kappa_z \eta_z}, \quad (\text{C29})$$

Then,

$$\begin{aligned} \delta\bar{\rho}_{\mathbf{q}_M+\mathbf{g}}^{\text{S,inter}} &= \sum_{\mathbf{k}_M} F_{\mathbf{q}_M}^{\text{S}}(\mathbf{k}_M) [e^{i\Phi_{\mathbf{q}_M}^{\text{S}}(\mathbf{k}_M)} (c_{A,o,K,\mathbf{k}_M}^\dagger c_{A,o',K,\mathbf{k}_M+\mathbf{q}_M} + c_{B,o',K,\mathbf{k}_M}^\dagger c_{B,o,K,\mathbf{k}_M+\mathbf{q}_M} - c_{A,o',K',\mathbf{k}_M}^\dagger c_{A,o,K',\mathbf{k}_M+\mathbf{q}_M} \\ &\quad - c_{B,o,K',\mathbf{k}_M}^\dagger c_{B,o',K',\mathbf{k}_M+\mathbf{q}_M}) + e^{-i\Phi_{\mathbf{q}_M}^{\text{S}}(\mathbf{k}_M)} (c_{A,o',K,\mathbf{k}_M}^\dagger c_{A,o,K,\mathbf{k}_M+\mathbf{q}_M} + c_{B,o,K,\mathbf{k}_M}^\dagger c_{B,o',K,\mathbf{k}_M+\mathbf{q}_M} \\ &\quad - c_{A,o,K',\mathbf{k}_M}^\dagger c_{A,o',K',\mathbf{k}_M+\mathbf{q}_M} - c_{B,o',K',\mathbf{k}_M}^\dagger c_{B,o,K',\mathbf{k}_M+\mathbf{q}_M})], \\ \delta\bar{\rho}_{-\mathbf{q}_M-\mathbf{g}}^{\text{S,inter}} &= \sum_{\mathbf{k}_M} F_{-\mathbf{q}_M}^{\text{S}}(\mathbf{k}_M) [e^{i\Phi_{-\mathbf{q}_M}^{\text{S}}(\mathbf{k}_M)} (c_{A,o,K,\mathbf{k}_M}^\dagger c_{A,o',K,\mathbf{k}_M-\mathbf{q}_M} + c_{B,o',K,\mathbf{k}_M}^\dagger c_{B,o,K,\mathbf{k}_M-\mathbf{q}_M} - c_{A,o',K',\mathbf{k}_M}^\dagger c_{A,o,K',\mathbf{k}_M-\mathbf{q}_M} \\ &\quad - c_{B,o,K',\mathbf{k}_M}^\dagger c_{B,o',K',\mathbf{k}_M-\mathbf{q}_M}) + e^{-i\Phi_{-\mathbf{q}_M}^{\text{S}}(\mathbf{k}_M)} (c_{A,o',K,\mathbf{k}_M}^\dagger c_{A,o,K,\mathbf{k}_M-\mathbf{q}_M} + c_{B,o,K,\mathbf{k}_M}^\dagger c_{B,o',K,\mathbf{k}_M-\mathbf{q}_M} \\ &\quad - c_{A,o,K',\mathbf{k}_M}^\dagger c_{A,o',K',\mathbf{k}_M-\mathbf{q}_M} - c_{B,o',K',\mathbf{k}_M}^\dagger c_{B,o,K',\mathbf{k}_M-\mathbf{q}_M})], \end{aligned}$$

Similar to the derivation of energy correction $\Delta E_{\text{type-1}}^A$. We take type-4 QH state with total Chern number $C_T = 1$ as example to calculate energy correction $\Delta E^S = \langle \psi^{(0)} | \mathcal{H}_I^{\text{S,inter}} | \psi^{(0)} \rangle$, and the wave function can be written as $|\Psi_{\text{type-4}}^{C=1}\rangle = \prod_{\mathbf{k}_M} c_{A,o,K,\mathbf{k}_M}^\dagger c_{A,o',K,\mathbf{k}_M}^\dagger c_{B,o,K,\mathbf{k}_M}^\dagger c_{B,o',K',\mathbf{k}_M}^\dagger |0\rangle$. Then, the derivation process is as follows

$$\begin{aligned} &\delta\bar{\rho}_{\mathbf{q}_M+\mathbf{g}}^{\text{S,inter}} |\Psi_{\text{type-4}}^{C=1}\rangle, \\ &= \sum_{\mathbf{k}_M} F_{\mathbf{q}_M}^{\text{S}}(\mathbf{k}_M) [e^{i\Phi_{\mathbf{q}_M}^{\text{S}}(\mathbf{k}_M)} c_{B,o',K,\mathbf{k}_M}^\dagger c_{B,o,K,\mathbf{k}_M+\mathbf{q}_M} - e^{-i\Phi_{\mathbf{q}_M}^{\text{S}}(\mathbf{k}_M)} c_{B,o',K',\mathbf{k}_M}^\dagger c_{B,o,K',\mathbf{k}_M+\mathbf{q}_M}] |\Psi_{\text{type-4}}^{C=1}\rangle, \\ &\delta\bar{\rho}_{-\mathbf{q}_M-\mathbf{g}}^{\text{S,inter}} |\Psi_{\text{type-4}}^{C=1}\rangle, \\ &= \sum_{\mathbf{k}_M} F_{-\mathbf{q}_M}^{\text{S}}(\mathbf{k}_M) [e^{i\Phi_{-\mathbf{q}_M}^{\text{S}}(\mathbf{k}_M)} c_{B,o',K,\mathbf{k}_M}^\dagger c_{B,o,K,\mathbf{k}_M-\mathbf{q}_M} - e^{-i\Phi_{-\mathbf{q}_M}^{\text{S}}(\mathbf{k}_M)} c_{B,o',K',\mathbf{k}_M}^\dagger c_{B,o,K',\mathbf{k}_M-\mathbf{q}_M}] |\Psi_{\text{type-4}}^{C=1}\rangle, \end{aligned} \quad (\text{C30})$$

where we can omit other terms due to the properties of fermions ($c^\dagger c^\dagger |0\rangle = 0$ and $c|0\rangle = 0$). Therefore, we obtain

$$\begin{aligned}
& \langle \Psi_{\text{type-4}}^{C=1} | \delta \bar{\rho}_{\mathbf{q}_M + \mathbf{g}}^S \delta \bar{\rho}_{-\mathbf{q}_M - \mathbf{g}}^S | \Psi_{\text{type-4}}^{C=1} \rangle, \\
& = \langle \Psi_{\text{type-4}}^{C=1} | \left\{ \sum_{\mathbf{k}'_M} F_{\mathbf{q}_M}^S(\mathbf{k}'_M) [e^{-i\Phi_{\mathbf{q}_M}^S(\mathbf{k}'_M)} c_{B,o,K,\mathbf{k}'_M}^\dagger c_{B,o',K,\mathbf{k}'_M + \mathbf{q}_M} - e^{i\Phi_{\mathbf{q}_M}^S(\mathbf{k}'_M)} c_{B,o,K',\mathbf{k}'_M}^\dagger c_{B,o',K',\mathbf{k}'_M + \mathbf{q}_M}] \right\} \\
& \quad \left\{ \sum_{\mathbf{k}_M} F_{-\mathbf{q}_M}^S(\mathbf{k}_M) [e^{i\Phi_{-\mathbf{q}_M}^S(\mathbf{k}_M)} c_{B,o',K,\mathbf{k}_M}^\dagger c_{B,o,K,\mathbf{k}_M - \mathbf{q}_M} - e^{-i\Phi_{-\mathbf{q}_M}^S(\mathbf{k}_M)} c_{B,o',K',\mathbf{k}_M}^\dagger c_{B,o,K',\mathbf{k}_M - \mathbf{q}_M}] \right\} | \Psi_{\text{type-4}}^{C=1} \rangle, \\
& = \langle \Psi_{\text{type-4}}^{C=1} | \left\{ \sum_{\mathbf{k}'_M} F_{\mathbf{q}_M}^S(\mathbf{k}'_M) [e^{-i\Phi_{\mathbf{q}_M}^S(\mathbf{k}'_M)} c_{B,o,K,\mathbf{k}'_M}^\dagger c_{B,o',K,\mathbf{k}'_M + \mathbf{q}_M}] \right\} \left\{ \sum_{\mathbf{k}_M} F_{-\mathbf{q}_M}^S(\mathbf{k}_M) [e^{i\Phi_{-\mathbf{q}_M}^S(\mathbf{k}_M)} c_{B,o',K,\mathbf{k}_M}^\dagger c_{B,o,K,\mathbf{k}_M - \mathbf{q}_M}] \right\} \\
& \quad + \left\{ \sum_{\mathbf{k}'_M} F_{\mathbf{q}_M}^S(\mathbf{k}'_M) e^{i\Phi_{\mathbf{q}_M}^S(\mathbf{k}'_M)} c_{B,o,K',\mathbf{k}'_M}^\dagger c_{B,o',K',\mathbf{k}'_M + \mathbf{q}_M} \right\} \left\{ \sum_{\mathbf{k}_M} F_{-\mathbf{q}_M}^S(\mathbf{k}_M) [e^{-i\Phi_{-\mathbf{q}_M}^S(\mathbf{k}_M)} c_{B,o',K',\mathbf{k}_M}^\dagger c_{B,o,K',\mathbf{k}_M - \mathbf{q}_M}] \right\} | \Psi_{\text{type-4}}^{C=1} \rangle, \\
& = \sum_{\mathbf{k}_M} \langle \Psi_{\text{type-4}}^{C=1} | \left\{ F_{\mathbf{q}_M}^S(\mathbf{k}_M - \mathbf{q}_M) [e^{-i\Phi_{\mathbf{q}_M}^S(\mathbf{k}_M - \mathbf{q}_M)} c_{B,o,K,\mathbf{k}_M - \mathbf{q}_M}^\dagger c_{B,o',K,\mathbf{k}_M}^\dagger] \right\} \left\{ F_{-\mathbf{q}_M}^S(\mathbf{k}_M) [e^{i\Phi_{-\mathbf{q}_M}^S(\mathbf{k}_M)} c_{B,o',K,\mathbf{k}_M}^\dagger c_{B,o,K,\mathbf{k}_M - \mathbf{q}_M}] \right\} \\
& \quad + \left\{ F_{\mathbf{q}_M}^S(\mathbf{k}_M - \mathbf{q}_M) e^{i\Phi_{\mathbf{q}_M}^S(\mathbf{k}_M - \mathbf{q}_M)} c_{B,o,K',\mathbf{k}_M - \mathbf{q}_M}^\dagger c_{B,o',K',\mathbf{k}_M}^\dagger \right\} \left\{ F_{-\mathbf{q}_M}^S(\mathbf{k}_M) [e^{-i\Phi_{-\mathbf{q}_M}^S(\mathbf{k}_M)} c_{B,o',K',\mathbf{k}_M}^\dagger c_{B,o,K',\mathbf{k}_M - \mathbf{q}_M}] \right\} | \Psi_{\text{type-4}}^{C=1} \rangle, \\
& = \sum_{\mathbf{k}_M} [F_{-\mathbf{q}_M}^S(\mathbf{k}_M)]^2 \langle \Psi_{\text{type-4}}^{C=1} | n_{B,o,K,\mathbf{k}_M - \mathbf{q}_M} (1 - n_{B,o',K,\mathbf{k}_M}) + n_{B,o,K',\mathbf{k}_M - \mathbf{q}_M} (1 - n_{B,o',K',\mathbf{k}_M}) | \Psi_{\text{type-4}}^{C=1} \rangle. \tag{C31}
\end{aligned}$$

In the second step, we have excluded terms that are inherently zero. Subsequently, in the third step, we substitute \mathbf{k}'_M with $\mathbf{k}_M - \mathbf{q}_M$. Finally, in the fourth step, we make use of the relationships as defined in Eq. C28.

Then, we can get

$$\Delta E_{\text{type-4}}^S = \frac{1}{2\Omega} \sum_{\mathbf{q}_M, \mathbf{k}_M, \mathbf{g}} V_{\mathbf{q}_M + \mathbf{g}} \langle \Psi_{\text{type-4}}^{C=1} | \delta \bar{\rho}_{\mathbf{q}_M + \mathbf{g}}^S \delta \bar{\rho}_{-\mathbf{q}_M - \mathbf{g}}^S | \Psi_{\text{type-4}}^{C=1} \rangle = 2\lambda_S \tag{C32}$$

where $\lambda_S = \frac{1}{2\Omega} \sum_{\mathbf{q}_M, \mathbf{k}_M, \mathbf{g}} V_{\mathbf{q}_M + \mathbf{g}} [F_{-\mathbf{q}_M}^S(\mathbf{k}_M)]^2$. Similarly, we can obtain the energy correction of other ground states induced by intrasublattice-interorbital interaction, shown in Table.S2.

We turn to consider energy correction induced by intrasublattice-interorbital interaction in IVC states. For IVC states with $C_T = \pm 2$, the flat band basis is transformed to $\psi_{\mathbf{k}_M}^\dagger = [c_{A,o,K}^\dagger, \frac{1}{\sqrt{2}}(e^{-i\phi/2}c_{A,o',K}^\dagger + e^{i\phi/2}c_{B,o',K'}^\dagger), c_{B,o,K}^\dagger, \frac{1}{\sqrt{2}}(e^{-i\phi/2}c_{B,o',K}^\dagger + e^{i\phi/2}c_{A,o',K'}^\dagger), c_{A,o,K'}^\dagger, \frac{1}{\sqrt{2}}(e^{-i\phi/2}c_{A,o',K}^\dagger - e^{i\phi/2}c_{B,o',K'}^\dagger), c_{B,o,K'}^\dagger, \frac{1}{\sqrt{2}}(e^{-i\phi/2}c_{B,o',K}^\dagger - e^{i\phi/2}c_{A,o',K'}^\dagger)]$. Then, the inter-orbital form factor becomes

$$\Lambda_{\pm \mathbf{q}_M \pm \mathbf{g}}^{\text{IVC},1}(\mathbf{k}_M) = \begin{pmatrix} 0 & \frac{e^{-i\phi/2}}{\sqrt{2}} \Delta_{\pm,1} & 0 & 0 & 0 & \frac{e^{-i\phi/2}}{\sqrt{2}} \Delta_{\pm,1} & 0 & 0 \\ \frac{e^{i\phi/2}}{\sqrt{2}} \Delta_{\pm,2} & 0 & 0 & 0 & 0 & 0 & -\frac{e^{-i\phi/2}}{\sqrt{2}} \Delta_{\pm,2} & 0 \\ 0 & 0 & 0 & \frac{e^{-i\phi/2}}{\sqrt{2}} \Delta_{\pm,1}^* & 0 & 0 & 0 & \frac{e^{-i\phi/2}}{\sqrt{2}} \Delta_{\pm,1}^* \\ 0 & 0 & \frac{e^{i\phi/2}}{\sqrt{2}} \Delta_{\pm,2}^* & 0 & -\frac{e^{-i\phi/2}}{\sqrt{2}} \Delta_{\pm,2}^* & 0 & 0 & 0 \\ 0 & 0 & 0 & -\frac{e^{i\phi/2}}{\sqrt{2}} \Delta_{\pm,1}^* & 0 & 0 & 0 & \frac{e^{i\phi/2}}{\sqrt{2}} \Delta_{\pm,1}^* \\ \frac{e^{i\phi/2}}{\sqrt{2}} \Delta_{\pm,2} & 0 & 0 & 0 & 0 & 0 & \frac{e^{-i\phi/2}}{\sqrt{2}} \Delta_{\pm,2} & 0 \\ 0 & -\frac{e^{i\phi/2}}{\sqrt{2}} \Delta_{\pm,1} & 0 & 0 & 0 & \frac{e^{i\phi/2}}{\sqrt{2}} \Delta_{\pm,1} & 0 & 0 \\ 0 & 0 & \frac{e^{i\phi/2}}{\sqrt{2}} \Delta_{\pm,2}^* & 0 & \frac{e^{-i\phi/2}}{\sqrt{2}} \Delta_{\pm,2}^* & 0 & 0 & 0 \end{pmatrix} \tag{C33}$$

Similar to the derivation process of Eq.C32, for $[\text{QH}]_o[\text{T-IVC}]_{o'}$ and $[\text{QH}]_o[\text{K-IVC}]_{o'}$ states, we can also derive their energy corrections induced by intrasublattice-interorbital interaction, as presented in Table.S3.

For IVC states with $C_T = 0$, the flat band basis can be transformed to $\psi_{\mathbf{k}_M}^\dagger = [\frac{1}{\sqrt{2}}(e^{-i\phi/2}c_{A,o,K}^\dagger + e^{i\phi/2}c_{B,o,K'}^\dagger), \frac{1}{\sqrt{2}}(e^{-i\phi/2}c_{A,o',K}^\dagger + e^{i\phi/2}c_{B,o',K'}^\dagger), \frac{1}{\sqrt{2}}(e^{-i\phi/2}c_{B,o,K}^\dagger + e^{i\phi/2}c_{A,o,K'}^\dagger), \frac{1}{\sqrt{2}}(e^{-i\phi/2}c_{B,o',K}^\dagger + e^{i\phi/2}c_{A,o',K'}^\dagger), \frac{1}{\sqrt{2}}(e^{-i\phi/2}c_{A,o,K}^\dagger - e^{i\phi/2}c_{B,o,K'}^\dagger), \frac{1}{\sqrt{2}}(e^{-i\phi/2}c_{A,o',K}^\dagger - e^{i\phi/2}c_{B,o',K'}^\dagger), \frac{1}{\sqrt{2}}(e^{-i\phi/2}c_{A,o,K}^\dagger - e^{i\phi/2}c_{B,o,K'}^\dagger), \frac{1}{\sqrt{2}}(e^{-i\phi/2}c_{A,o',K}^\dagger - e^{i\phi/2}c_{B,o',K'}^\dagger)]$.

$C_T = \pm 2$	Q_1^2 $\kappa_z \mu_0 \eta_0$	Q_2^2 $\kappa_z \mu_z \eta_0$	Q_3^2 $[\kappa_z \mu_z] \oplus [\kappa_z \mu_0]$	Q_4^2 $[\kappa_z \mu_0] \oplus [\kappa_z \mu_z]$	Q_5^2 $[\kappa_z \oplus \mu_z] \oplus [\kappa_z \oplus (-\mu_0)]$	Q_6^2 $[\kappa_z \oplus (-\mu_0)] \oplus [\kappa_z \oplus \mu_0]$
$C_T = \pm 1$	Q_1^1 $[\kappa_0 \mu_z] \oplus [\kappa_z \mu_z]$	Q_2^1 $[\kappa_z \mu_z] \oplus [-\kappa_0 \mu_z]$	Q_3^1 $[-\kappa_0 \mu_z] \oplus [\kappa_z \mu_z]$	Q_4^1 $[\kappa_0 \oplus \mu_z] \oplus [\kappa_z \oplus (-\mu_0)]$		
	Q_5^1 $[\kappa_0 \mu_z] \oplus [\kappa_z \mu_0]$	Q_6^1 $[\kappa_0 \oplus (-\mu_z)] \oplus [\kappa_z \oplus (-\mu_0)]$	Q_7^1 $[\kappa_z \mu_0] \oplus [\kappa_0 \mu_z]$	Q_8^1 $[\kappa_z \oplus (-\mu_0)] \oplus [\kappa_0 \oplus \mu_z]$		
	Q_9^1 $[\kappa_z \mu_z] \oplus [\kappa_0 \mu_z]$	Q_{10}^1 $[\kappa_z \oplus (-\mu_0)] \oplus [\kappa_0 \oplus (-\mu_z)]$	Q_{11}^1 $[\kappa_z \oplus \mu_0] \oplus [(-\kappa_0) \oplus \mu_z]$	Q_{12}^1 $[\kappa_z \mu_0] \oplus [-\kappa_0 \mu_z]$		
	Q_{13}^1 $[\kappa_z \oplus \mu_0] \oplus [-\kappa_0 \oplus \mu_z]$	Q_{14}^1 $[-\kappa_0 \mu_z] \oplus [\kappa_z \mu_0]$	Q_{15}^1 $[(-\kappa_0) \oplus \mu_z] \oplus [\kappa_z \oplus \mu_0]$	Q_{16}^1 $[-\kappa_0 \oplus \mu_z] \oplus [\kappa_z \oplus \mu_0]$		
$C_T = 0$	Q_1^0 $\kappa_0 \mu_0 \eta_z$	Q_2^0 $-\kappa_0 \mu_0 \eta_z$	Q_3^0 $\kappa_0 \mu_z \eta_0$	Q_4^0 $-\kappa_0 \mu_z \eta_0$		
	Q_5^0 $\kappa_0 \mu_z \eta_z$	Q_6^0 $-\kappa_0 \mu_z \eta_z$	Q_7^0 $\kappa_z \mu_0 \eta_z$	Q_8^0 $\kappa_z \mu_z \eta_z$		
	Q_9^0 $[\kappa_z \mu_0] \oplus [-\kappa_z \mu_z]$	Q_{10}^0 $[\kappa_z \mu_z] \oplus [-\kappa_z \mu_0]$	Q_{11}^0 $[\kappa_z \oplus \mu_0] \oplus [-\kappa_z \oplus \mu_0]$	Q_{12}^0 $[\kappa_z \oplus (-\mu_0)] \oplus [(-\kappa_z) \oplus \mu_0]$		
	Q_{13}^0 $[\kappa_0 \oplus \mu_z] \oplus [-\kappa_0 \oplus \mu_z]$	Q_{14}^0 $[(-\kappa_0) \oplus \mu_z] \oplus [\kappa_0 \oplus (-\mu_z)]$	Q_{15}^0 $[\kappa_0 \oplus \mu_z] \oplus [(-\kappa_0) \oplus \mu_z]$	Q_{16}^0 $[(-\kappa_0) \oplus \mu_z] \oplus [\kappa_0 \oplus \mu_z]$		

TABLE S4: Operators $Q_n^{|C_T|}$ for each ground state.

$e^{i\phi/2} c_{A,o,K'}^\dagger$, $\frac{1}{\sqrt{2}}(e^{-i\phi/2} c_{B,o',K}^\dagger - e^{i\phi/2} c_{A,o',K'}^\dagger)$. Then, the inter-orbital form factor becomes

$$\Lambda_{\pm \mathbf{q}_M \pm \mathbf{g}}^{\text{IVC},2}(\mathbf{k}_M) = \begin{pmatrix} 0 & 0 & 0 & 0 & 0 & \Delta_{\pm,1} & 0 & 0 \\ 0 & 0 & 0 & 0 & \Delta_{\pm,2} & 0 & 0 & 0 \\ 0 & 0 & 0 & 0 & 0 & 0 & 0 & \Delta_{\pm,1}^* \\ 0 & 0 & 0 & 0 & 0 & 0 & \Delta_{\pm,2}^* & 0 \\ 0 & \Delta_{\pm,1} & 0 & 0 & 0 & 0 & 0 & 0 \\ \Delta_{\pm,2} & 0 & 0 & 0 & 0 & 0 & 0 & 0 \\ 0 & 0 & 0 & \Delta_{\pm,1}^* & 0 & 0 & 0 & 0 \\ 0 & 0 & \Delta_{\pm,2}^* & 0 & 0 & 0 & 0 & 0 \end{pmatrix}, \quad (\text{C34})$$

Similarly, for $[\text{T-IVC}]_o[\text{T-IVC}]_{o'}$, $[\text{T-IVC}]_o[\text{K-IVC}]_{o'}$, $[\text{K-IVC}]_o[\text{I-IVC}]_{o'}$ and $[\text{K-IVC}]_o[\text{K-IVC}]_{o'}$ states, we can also obtain their energy corrections induced by intrasublattice-interorbital interaction, as shown in Table.S3.

d. Intuitive picture about the energy correction

Here, we will present an intuitive picture to understand the energy correction resulting from the above single-particle dispersion and two interactions, and the eight flat bands can be organized into four pairs of bands connected by these three terms (denoted by red curves, green and blue wavy lines in Fig.(S11-S13)). The single-particle dispersion describes the hopping channels between one pair of bands connected by single-particle term. On the other hand, energy corrections arising from these two

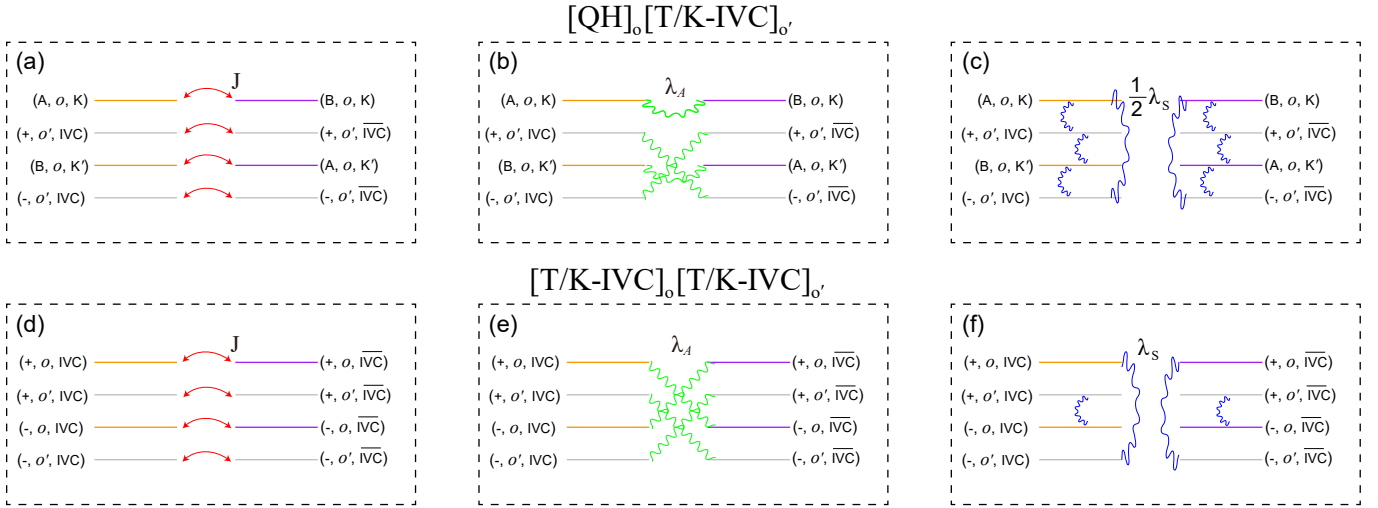


FIG. S16: (color online) Schematic illustration of single-particle dispersion (red curves), intersublattice-intraorbital (green wavy lines) and intrasublattice-interorbital (blue wavy lines) interactions in the basis of IVC states for $[\text{QH}]_o[\text{T/K-IVC}]_{o'}$ and $[\text{T/K-IVC}]_o[\text{T/K-IVC}]_{o'}$ states. The parameters of J , λ_A and λ_S are the strength of the corresponding perturbation within the basis of IVC states.

interactions are proportional to $\lambda_{A/S}\hat{n}(1 - \hat{n}')$, where \hat{n} and \hat{n}' represent the particle number operators for the pair of bands linked by the corresponding interactions. Then, we can summarize three distinct scenarios regarding energy corrections: (i) In a state, when all four pairs of bands connected by these terms are fully occupied or fully empty, the energy corrections vanish due to the absence of allowed hopping and interaction channels. In VP in Fig.S13 (a) and (b), this applies to the four pairs of bands connected by these three terms, and the energy corrections are zero shown in Table.S2. (ii) In a state, where each pair of bands connected by the perturbation term is half-filled, the hopping and interacting channels between each pair of bands are allowed, resulting four-fold such energy correction. In type-2 and -2' QH states in Fig.S11 (b), all four pairs of bands belong to this category and the energy corrections are $\Delta E = 4\lambda_A + 4\lambda_S - 4J$ in Table.S2. (iii) In a state, where two of the four pairs connected by these terms are either occupied or empty while the other two pairs are half-filled, two-fold such energy correction is generated. In type-(5~6) and -(5' ~ 6') QH states in Fig.S11 (e) and (f), all four pairs of bands belong to this case and the energy corrections are $\Delta E = 2\lambda_A + 2\lambda_S - 2J$ in Table.S2. Finally, Table.S2 presents energy correction for each ground state, and the energy correction can be expressed by a general formula as

$$\Delta E = N_A\lambda_A + N_S\lambda_S - N_JJ, \quad (\text{C35})$$

where the parameters $N_{A/S/J}$ are determined by the number of allowing hopping and interacting channels. It is noteworthy that the single-particle Hamiltonian and the inter-Chern-number interaction establish connections between the same pairs of bands, resulting in $N_A = N_J$.

To characterize each ground state identified by the number n and total Chern number C_T , we introduce a corresponding operator denoted as $Q_n^{|C_T|}$. This operator possesses the property of $Q_n^{|C_T|}|\Psi_n^{C_T}\rangle = \pm|\Psi_n^{C_T}\rangle$, where $|\Psi_n^{C_T}\rangle$ represents the wave function of the ground state. We can determine the values of the parameters $N_{A/S/J}$ by utilizing the commutation relations between $Q_n^{|C_T|}$ and x , where x denotes the single-particle dispersion h in Eq.C10, the form factor Λ^A in Eq.C20 and the form factor $\Lambda^{S,\text{inter}}$ in Eq.C29. When the commutation relation is a commutator or an anticommutator, these parameters take values of either 0 or 4. However, when the commutation relation is neither a commutator nor an anticommutator, these parameters take a value of 2. Table.S4 presents the corresponding operator $Q_n^{|C_T|}$ for each ground state.

In addition, the general formula Eq.C35 for the energy correction, which are determined by the number of allowed hopping and interacting channels, can also be applied to IVC states in Table.S3. In analogy to the schematic depiction of the three perturbations in Fig.S11-S13, Fig.S16 also provides the schematic illustration of single-particle dispersion (red curves), intersublattice-intraorbital (green wavy lines) and intrasublattice-interorbital (blue wavy lines) interactions within the basis of IVC states. For $[\text{T/K-IVC}]_o[\text{T/K-IVC}]_{o'}$ states, the strengths of the three perturbations within the basis of IVC states remain invariant, as shown in Fig.S16(d)-(f). However, in $[\text{QH}]_o[\text{T/K-IVC}]_{o'}$ states, the strength and channel of intrasublattice-interorbital interaction are halved and doubled, respectively, as depicted in Fig.S16(c). In type-1 state of $[\text{QH}]_o[\text{T-IVC}]_{o'}$ in Fig.S14(a), the number of allowing channels for single-particle dispersion, intersublattice-intraorbital and intrasublattice-interorbital interactions are two, four and two, and hence $\Delta E=4\lambda_A+2\lambda_S-2J$. In type-4 state of $[\text{K-IVC}]_o[\text{K-IVC}]_{o'}$ in Fig.S15(p), the number of

allowing channels for corresponding perturbation are four, zero and zero, and hence $\Delta E = -4J$.

- [1] G. Tarnopolsky, A. J. Kruchkov, and A. Vishwanath, *Phys. Rev. Lett.* 122, 106405 (2019).
 - [2] Z.-D. Song, B. Lian, N. Regnault, and B. A. Bernevig, *Phys. Rev. B* 103, 205412 (2021).
 - [3] D. Mumford, *Tata Lectures on Theta I*, *Progress in Mathematics* (1983), Vol. 28, pp. XIII, 240.
 - [4] B. Andrei Bernevig, Zhi-Da Song, Nicolas Regnault, and Biao Lian, *Phys. Rev. B* 103, 205413 (2021).
 - [5] Patrick J. Ledwith, Eslam Khalaf, Ashvin Vishwanath, *Annals of Physics* 435 (2021) 168495.
 - [6] Nick Bultinck, Eslam Khalaf, Shang Liu, Shubhayu Chatterjee, Ashvin Vishwanath, and Michael P. Zaletel, *Phys. Rev. X* 10, 031034 (2020).
-